Introduction and application of a drive-by damage detection methodology for bridges using variational mode decomposition

Shahrooz Khalkhali Shandiz, Hamed Khezrzadeh
Faculty of Civil and Environmental Engineering, Tarbiat Modares University, Jalal Ale Ahmad Highway, P.O. Box 14115-143, Tehran, Iran;
k.shahrooz@modares.ac.ir
khezrzadeh@modares.ac.ir, https://orcid.org/0000-0002-7248-2083

Saeed Eftekhar Azam
Department of Civil and Environmental Engineering, University of New Hampshire, 33 Academic Way, W 137, Durham, 03824, NH, USA
Saeed.EftekharAzam@unh.edu https://orcid.org/0000-0001-8153-5506

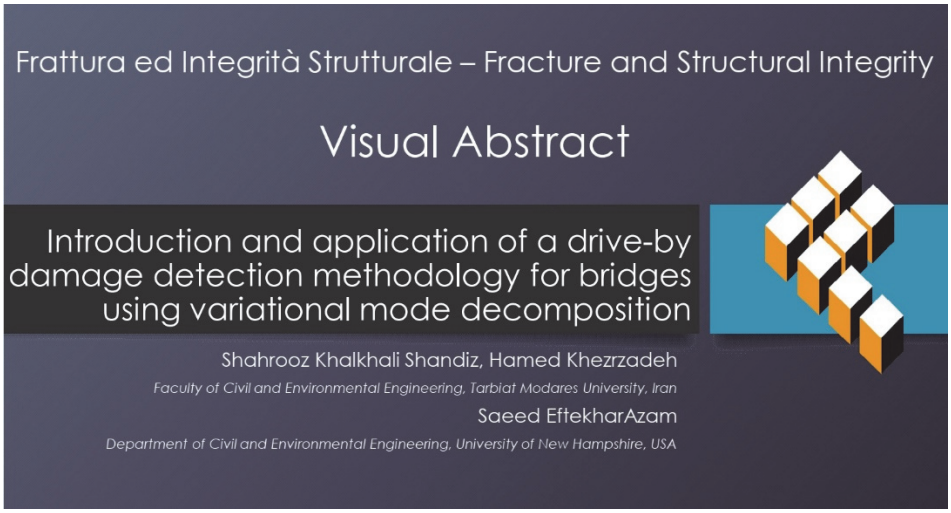

Citation: Shandiz, S.K., Khezrzadeh, H., Azam, S.E., Introduction and application of a drive-by damage detection methodology for bridges using variational mode decomposition, Frattura ed Integrità Strutturale, 70 (2024) 24-54.

Received: 09.04.2024
Accepted: 30.06.2024
Published: 09.07.2024
Issue: 10.2024

KEYWORDS. Structural Health Monitoring (SHM), Drive-by sensing, Indirect damage detection, Variational Mode Decomposition (VMD) method, Signal processing, Finite Element Method (FEM).

INTRODUCTION

Bridges, as one of the most crucial parts of transportation infrastructure, need constant monitoring to ensure their serviceability. Visual inspection is one of the conventional methods of structural health monitoring (SHM) in bridges. Nevertheless, the damages cannot be detected through this method when they are not visible. Because of the inefficiency in identifying potential defects in this method [1], researchers have tried other ways for direct monitoring. In general, there are four classifications of structural damage detection. At the first level, the major concern is detecting the presence of damage while at the second level, the location of the damage is of interest. The damage frequency and severity

are estimated at the third level, and the structure's remaining life is assessed at the fourth level [2]. Vibration-based approaches are used in bridge health monitoring by placing sensors at a limited number of points of the bridge structure and collecting data derived from these sensors [3–5]. In order to determine the bridge's dynamic properties as well as damage detection, these output data are examined and interpreted. This technique is categorized as a direct method of health monitoring [6]. These sensors measure strains, accelerations, temperatures, and other parameters which are prominent indicators of the structures' health state [7]. Extensive research has been done on this subject. Lee and Shin [8] applied a two-step method using a frequency response function-based and reduced-domain method to find damage zones on a beam. Recent studies have utilized state estimation and the Dual Kalman filter to detect damage and fatigue in structures caused by vibration [9]. The use of Artificial Intelligence and big data to overcome the enormous data obtained from the installed sensors is reviewed in [10]. The application of Proper Orthogonal Decomposition (POD) [11,12] and Artificial Neural Networks (ANNS) to spot damage locations on railway bridges subjected to unknown loads is investigated in [13,14]. One of the other applications of machine learning in vibration-based techniques is the early detection of bridge damage through the use of unsupervised learning techniques [15].

In contrast to the direct SHM methods, which are generally demanding in terms of resources and workforce, the indirect methods of health monitoring are considered substantially more economical. In the indirect SHM techniques, the collected moving vehicle signals are analyzed to assess structural health conditions. The indirect method is an economical solution because fewer sensors than the direct methods are required. The other merit of using indirect techniques is that the device can be adapted and used in the SHM of different bridge structures. Primarily, the indirect method was used to reach an estimate of bridge vibration frequencies in [16–18]. In these studies, the bridge is modeled as an Euler-Bernoulli beam and the vehicle as a moving oscillator, and it was observed that the two major vehicle frequencies are the ones that have been shifted by $\pi v/L$ where v is the moving vehicle's speed and L is the bridge span. The impacts of irregularity on frequency are also investigated in these studies. In order to eliminate the limitation of using single vibration mode, Fourier transform and EMD were applied in [19] to include the effects of higher vibration modes. Many researchers have tried to develop theoretical methods for comparing results with experimental studies [20,21], e.g. in [22], the predictions of [16,17] were tested by a truck passing over a bridge in Taiwan, indicating that low speed for determining the bridge's frequency provides better results in comparison to high passing speeds. There have been studies carried out through the indirect method to obtain the bridge damping, and its influence on the vehicle vibration [23,24], the conclusions are validated experimentally in scaled laboratory tests [25,26]. Bridge mode shapes can be utilized as a valuable tool in improving a bridge's model [27], to determine the mode shapes of the bridge, researchers used techniques such as short-time frequency transformation [28], singular value decomposition [29], Hilbert and Hilbert-Huang transform [30–32], and Fourier transformation [33].

In addition to the application of the indirect method in characterizing the dynamic properties of the structure, this method can be implemented in detecting structural damage. Damage could result in the degradation of the bridge stiffness or a change in its geometry, causing fluctuations in vehicle vibration. Bu et al. [34] measured the dynamic response of the vehicle moving on deck modeled using Euler-Bernoulli's theory, where a reduction in beam stiffness was applied as a damage indicator; followingly, damages were detected using the Regularization technique. Kim and Kawatani [35] also conducted a laboratory experiment and found that drive-by sensing is effective in estimating damage location and severity. The wavelet transform is a mathematical technique that is frequently utilized in signal processing applications with the ability to identify specific patterns concealed in large amounts of data [36]. In different research studies (e.g., see [37–39]), this approach was utilized to detect anomalies in the vibration signals of moving vehicles. It was found that analyzing wavelet coefficients as damage indices will give clues about the damage locations in bridges. The wavelet spectrum was used to detect the location of open and breathing cracks in [40]. In this context, the instantaneous frequency of the beam, as determined by the wavelet spectrum, remains constant in the presence of open cracks, but varies if breathing cracks are present. The case of simultaneous bridge deck damage and a reduction in cable tension in cable-stayed bridges was studied in [41] in which for the vehicle's relative displacement response vector, the vertical displacement of the vehicle in a damaged and healthy bridge is used to generate the response vector.

EMD as a time-frequency technique created by Huang in the 1990s is utilized in a variety of disciplines [56], such as defect diagnostics of roller bearings [57], price forecasting in economic concerns [58], wind speed prediction [59], and more. In an effort to use EMD in bridge damage detection, the work by E.J. Obrien et al. [42] can be highlighted. The decomposition of the displacement vector based on POD indicates the location of the damage in the diagrams. To reach the damage location, the EMD technique used a signal derived from the difference between the vehicle's vertical displacement in healthy and damaged circumstances. By examining two indications of vehicle acceleration spectrum and change in bridge displacement, a novel technique of bridge damage detection was developed [43]. In the indirect damage diagnosis procedure, eliminating surface roughness impacts is a challenging issue. Surface irregularity leads to unpredictable vibrations, making damage diagnosis more difficult. Li et al. [44] employed the Dual Kalman Filter to assess surface irregularity. The damage

zone was determined by applying Tikhonov Regularization on the contact force between the vehicle and the bridge. The method's accuracy is validated against laboratory data. It is noteworthy that selecting the appropriate settings for wavelet transform to identify the abnormality of signals caused by structural defects is of essential importance. Using the wavelet entropy method to determine the optimal wavelet scale was explored in [45].

Applying vehicle and bridge interaction in a large-scale cable bridge to fill the gap between simple modeling and realistic modeling was done in [46]. Consequently, EMD was employed in the identification of damage caused by reduced cable stiffness, while the influence of various vehicle characteristics and road irregularities was also explored. In order to achieve an instantaneous frequency of the acceleration signal of two stationary and moving sensors, which are at a chosen position on the beam and on a moving oscillator, respectively, the EMD approach and the Hilbert transform were examined [47]; a jump in instantaneous frequency signals indicated damage location.

VDM as a recently developed method for signal processing is noticed by researchers in various fields Electromechanics [48], fluid mechanics [49], and economics [50]. The implementation of VMD for modal identification such as natural frequencies, damping ratio, and mode shapes in a structural system was investigated in [51,52]. Moreover, utilizing the VMD approach in combination with the band-pass filter (BPF) method to estimate the frequency of the structure using the contact-point response has demonstrated its efficiency once compared to other methods such as EMD [53]. Employing VMD as a technique for signal decomposition of a moving oscillator on a simply supported beam was studied in [54]. They conducted a comparative investigation with the EMD approach, indicating that, unlike EMD, the VMD method can identify damages without any baseline of a healthy beam.

A novel approach in the field of Structural Health Monitoring (SHM) is introduced by employing VMD for drive-by damage detection in bridges. Despite using VMD as a method in SHM, the advantage of this work lies in considering various influencing factors analytically. A comprehensive parametric study is conducted, with VMD utilized in drive-by sensing and critical parameters such as crack depth, road roughness, noise, and vehicle velocity investigated. Unlike previous research that relies on simpler vehicle models, a more complex vehicle model is incorporated, enhancing its applicability to real-world scenarios. The damage detection process is simplified, and its robustness against various uncertainties is increased by the approach. Damage is effectively identified by the VMD method even under challenging conditions, such as rough road surfaces and significant ambient noise, while computational efficiency is maintained. Additionally, a method is applied to significantly reduce the impact of road roughness on signals, improving the reliability of the results. A finite element code is developed in MATLAB® to analyze the interaction between a trailer-tractor (TT) and the bridge, modeled as a half-car and an Euler-Bernoulli beam, respectively. This code is validated against modal analysis data, with responses compared and crack-type damage incorporated based on fracture mechanics concepts. Various irregularity conditions, crack depths, velocities, and noise effects are investigated to assess the efficiency of the VMD method in these scenarios. The unique aspects of this theoretical parametric study provide a robust foundation for future practical studies on implementing VMD as a valuable tool in the SHM domain.

The article is structured as follows: an overview and fundamentals of EMD and VMD are presented in the Signal Processing section. The proposed method is described in detail in the Proposed Methodology section, where the vehicle-bridge interaction relationships are given by applying two procedures: modal and finite element analysis, and the relationship of the damaged element and the application of surface irregularity and finally, the vibration signal of the vehicle are also discussed. In the Results and Discussions section, the acquired bridge signals are analyzed through EMD and VMD in search of damage location(s), and the sensitivity of the damage detection methodology is examined through various influential factors such as different damage locations and severity, presence of surface irregularities, various trailer masses, and ambient noise. Finally, the Conclusion section summarizes the key findings and contributions of this study.

SIGNAL PROCESSING

Time-frequency techniques enhance the representation of non-stationary vibration data [55]. EMD breaks down a signal by decomposing it backward into modes. Methodically, modes have their own frequency spectra. However, this technique has certain drawbacks, including noise sensitivity and sample frequency [60]. The VMD, as a recently developed technique, is mathematically more reliable. It is indicated in [61] that using the VMD better results can be reached with less computing complexity at significantly lower levels of residual noise in the modes.

Empirical Mode Decomposition

As stated, in the EMD the signal is decomposed into modes, also known as IMFs (Intrinsic Mode Functions). Each IMF must meet two requirements:

- The number of extrema and zero-crossings is exactly/nearly the same.
- The mean value of the envelopes is defined by the local maxima and the local minima is zero at any point.

The EMD procedure requires spline fitting to create the upper and lower envelopes of the signal and compute the mean of both envelopes. The signal is then subtracted from the mean, which is called the sifting process. The process is repeated until the resultant signal meets the mentioned requirements, at which point it is considered as an IMF. After subtracting the IMF from the original signal, the sifting process is repeated on the remaining signal to yield further IMFs [19,56] (see Fig. 1a).

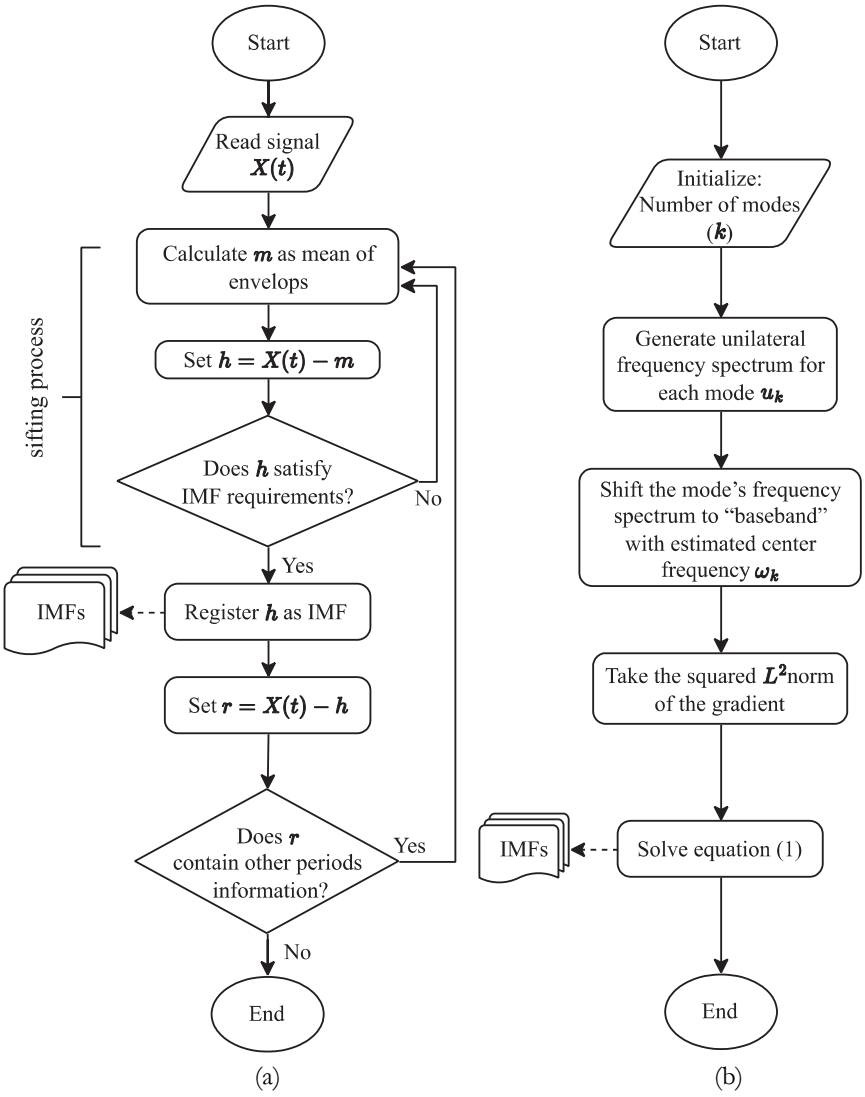

Figure 1: (a) EMD, (b) VMD flowchart.

Variational Mode Decomposition

A new method to break down the signal into its elemental components called VMD was introduced by Dragomiretskiy and Zosso [60]. This method is based on Wiener filtering, Hilbert transforms, analytic signal and frequency mixing, and heterodyne demodulation. In this method, a completely non-reversible VMD model is presented, in which the modes are extracted in one step (see Fig. 1b). The purpose of this method is to obtain a set of modes and their corresponding central frequencies so that the sum of the modes retrieves the input signal. Each sub-signal is supposed to be compressed around a corresponding central frequency ω_k which is extracted using the method. The decomposed signals are called IMF. An IMF is defined as an Amplitude-Modulated-Frequency-Modulated (AM-FM) adaptively in the frequency domain by VMD. By considering the adequate number of modes for VMD, the abnormality in the signals can be captured successfully.

Incorporating the Wiener filter makes the VMD noise-resistant as indicated in [60]. The VMD equation is expressed as follows:

$$\mathcal{L}(\{u_k\},\{\omega_k\},\lambda)=\alpha\sum_k\left\|\partial_t\left[\left(\delta(t)+\frac{j}{\pi t}\right)*\boldsymbol{u}_k(t)\right]e^{-j\omega_k t}\right\|_2^2+\left\|\boldsymbol{f}(t)-\sum_k\boldsymbol{u}_k(t)\right\|_2^2+\langle\boldsymbol{\lambda}(t),\boldsymbol{f}(t)-\sum_k\boldsymbol{u}_k(t)\rangle \quad (1)$$

where α expresses the variance of white noise, δ is the Dirac delta function, j is equal to $\sqrt{-1}$, $\boldsymbol{f}(t)$ denotes the original signal, $\boldsymbol{\lambda}$ is the Lagrange's multiplier, and $*$ represents the convolution sign. The abbreviated representations of all modes and their central frequencies are given by $\{\boldsymbol{u}_k\}=\{u_1,\cdots,u_k\}$ and $\{\boldsymbol{\omega}_k\}=\{\omega_1,\cdots,\omega_k\}$, respectively [60]. The instantaneous energy of each mode is given as:

$$\mathrm{IE}=\int_0^{\omega_N}H^2(t,\omega)d\omega \quad (2)$$

where ω_N represents the desired IMF frequency and H represents the Hilbert transform of each mode [62].

PROPOSED METHODOLOGY

In this section, a novel methodology for the indirect locating of cracks is proposed. A single-axis device is connected to a truck passing the bridge in the proposed method. The selection of a single-axis device is due to its high flexibility in adjusting its physical characteristics, which is a different damage detection apparatus in comparison to previous studies [37,63]. Consequently, the increased degrees of device freedom need the development of a new set of equations, which is derived hereafter. Vehicle-bridge interaction equations are verified in comparison with the modal analysis in the Finite element method and Modal analysis method section. The damaged element relationships are given for a self-contained presentation in the Damaged element section. The validity and accuracy of these relationships are checked by comparing results for the frequencies attained in the experimental test and numerical simulation of the pre-cracked beam. The relationships employed to model surface irregularities are also explicitly described in the Road surface profiles section. To minimize the influence of surface irregularities on crack detection, a novel method for acquiring signals from the vehicle was proposed in the Vibration signal section. The overall procedure of the proposed method is summarized in Fig. 2.

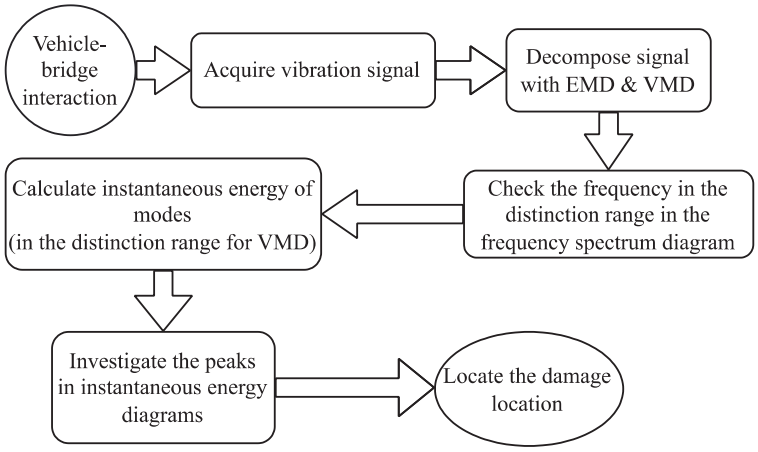

Figure 2: Proposed method schematic.

Finite element method

In this section, the equations defining the interaction of TT and bridge in the finite element code are presented. The instrument employed here is a more detailed and realistic replica of the commonly used devices in some previous studies [37,40,63–65]. The vehicle has been outfitted with a trailer system. A schematic diagram of the trailer-tractor passing a bridge

is shown in Fig. 3. The schematic of the 6 Degrees of Freedom (DoF) TT assembly which will be used as a signal acquisition vehicle is shown in Fig. 4a. The dynamic equation of TT vibration can be written as follows:

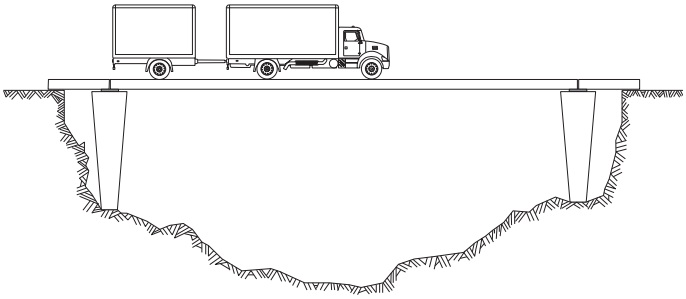

Figure 3: Tractor and trailer (TT).

$$[\mathbf{M_T}]\{\ddot{d}\}+[\mathbf{C_T}]\{\dot{d}\}+[\mathbf{K_T}]\{d\}=\{F_T\} \tag{3}$$

The mass, damping, stiffness, and force matrices are presented in Appendix A.

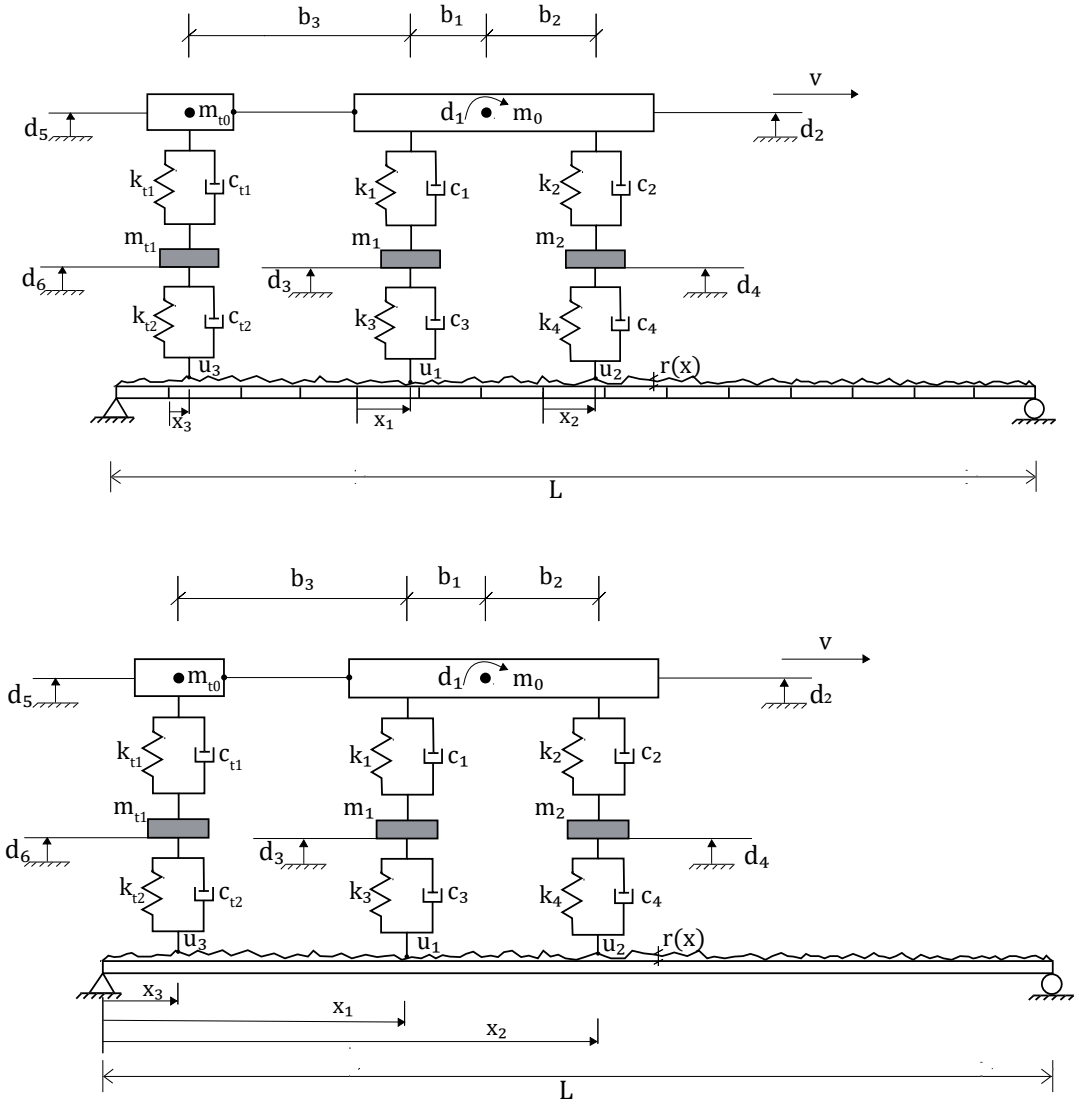

Figure 4: Bridge and TT's degrees of freedom in (Top) FEM, (Bottom) Modal Analysis Method.

The bridge vibration equation as an Euler-Bernoulli beam with two simple ends and 3-point contact with TT is given as:

$$[\mathbf{M}_b]\{\ddot{\boldsymbol{d}}\}+[\mathbf{C}_b]\{\dot{\boldsymbol{d}}\}+[\mathbf{K}_b]\{\boldsymbol{d}\}=[\mathbf{N}_1]^T\boldsymbol{f}_1+[\mathbf{N}_2]^T\boldsymbol{f}_2+[\mathbf{N}_3]^T\boldsymbol{f}_t \tag{4}$$

$$\boldsymbol{f}_1=-m_1\boldsymbol{g}+m_1\ddot{\boldsymbol{d}}_3-\frac{m_0\boldsymbol{g}b_2}{b_1+b_2}+\frac{I_0\ddot{\boldsymbol{d}}_1+m_0b_2\ddot{\boldsymbol{d}}_2}{b_1+b_2} \tag{5}$$

$$\boldsymbol{f}_2=-m_2\boldsymbol{g}+m_2\ddot{\boldsymbol{d}}_4-\frac{m_0\boldsymbol{g}b_1}{b_1+b_2}+\frac{I_0\ddot{\boldsymbol{d}}_1+m_0b_1\ddot{\boldsymbol{d}}_2}{b_1+b_2} \tag{6}$$

$$\boldsymbol{f}_t=-m_{t1}\boldsymbol{g}+m_{t0}\ddot{\boldsymbol{d}}_5 \tag{7}$$

where $\boldsymbol{f}_1$, $\boldsymbol{f}_2$, and $\boldsymbol{f}_t$ are the interaction forces at the rear, front, and trailer axle, respectively. The displacement of the beam $\boldsymbol{u}$ at an arbitrary point such as x is obtained using the shape function [**N**] and the displacement of the node $\boldsymbol{d}$ [66]:

$$\boldsymbol{u}=[\mathbf{N}]\{\boldsymbol{d}\} \tag{8}$$

The beam element shape function is given as:

$$[\mathbf{N}]=\begin{bmatrix}N_1 & N_2 & N_3 & N_4\end{bmatrix} \tag{9}$$

where shape function components are defined by the following well-known relations:

$$N_1=1-3\left(\frac{x}{l}\right)^2+2\left(\frac{x}{l}\right)^3,\quad N_2=x\left(\frac{x}{l}-1\right)^2,\quad N_3=3\left(\frac{x}{l}\right)^2-2\left(\frac{x}{l}\right)^3,\quad N_4=x\left[\left(\frac{x}{l}\right)^2-\frac{x}{l}\right] \tag{10}$$

The derivative of $\boldsymbol{u}$ with respect to time is defined as:

$$\dot{\boldsymbol{u}}(x,t)=\frac{\partial\boldsymbol{u}}{\partial x}\dot{\boldsymbol{x}}+\frac{\partial\boldsymbol{u}}{\partial t} \tag{11}$$

Given that [**N**] is a location-dependent function and $\boldsymbol{d}$ is time-dependent, according to Eqn. 8:

$$\frac{\partial\boldsymbol{u}}{\partial x}=[\mathbf{N}]_x\boldsymbol{d} \tag{12}$$

By placing Eqn. (11) and Eqn. (12) into Eqn. (3) and Eqn. (4), the trailer-tractor and bridge interaction equation can be reached as:

$$[\mathbf{M}]\{\ddot{\boldsymbol{d}}\}+[\mathbf{C}]\{\dot{\boldsymbol{d}}\}+[\mathbf{K}]\{\boldsymbol{d}\}=\{\boldsymbol{F}\} \tag{13}$$

The matrices [**M**], [**C**], and [**K**] are defined as follows:

$$[\mathbf{M}]=\begin{bmatrix} [\mathbf{M}_b] & \sum_{i=0}^{2}[\mathbf{N}_i]^T \boldsymbol{f}_{\theta i} & \sum_{i=0}^{2}[\mathbf{N}_i]^T \boldsymbol{f}_{yi} & m_1[\mathbf{N}_1]^T & m_2[\mathbf{N}_2]^T & \sum_{i=0}^{2}[\mathbf{N}_i]^T \boldsymbol{f}_{yt} & m_{t1}[\mathbf{N}_3]^T \\ [0] & I_0 & 0 & 0 & 0 & 0 & 0 \\ [0] & 0 & m_0 & 0 & 0 & 0 & 0 \\ [0] & 0 & 0 & m_1 & 0 & 0 & 0 \\ [0] & 0 & 0 & 0 & m_2 & 0 & 0 \\ [0] & 0 & 0 & 0 & 0 & m_{t0} & 0 \\ [0] & 0 & 0 & 0 & 0 & 0 & m_{t1} \end{bmatrix} \tag{14}$$

$$[\mathbf{C}]=\begin{bmatrix} [\mathbf{C}_b] & \{0\} & \{0\} & \{0\} & \{0\} & \{0\} & \{0\} \\ [0] & c_1b_1^2+c_2b_2^2 & c_1b_1-c_2b_2 & -c_1b_1 & c_2b_2 & 0 & 0 \\ [0] & c_1b_1-c_2b_2 & c_1+c_2 & -c_1 & -c_2 & 0 & 0 \\ -c_3[\mathbf{N}_1] & -c_1b_1 & -c_1 & c_1+c_3 & 0 & 0 & 0 \\ -c_4[\mathbf{N}_2] & c_2b_2 & -c_2 & 0 & c_2+c_4 & 0 & 0 \\ [0] & 0 & 0 & 0 & 0 & c_{t1} & -c_{t1} \\ -c_{t2}[\mathbf{N}_3] & 0 & 0 & 0 & 0 & -c_{t1} & c_{t1}+c_{t2} \end{bmatrix} \tag{15}$$

$$[\mathbf{K}]=\begin{bmatrix} [\mathbf{K}_b] & \{0\} & \{0\} & \{0\} & \{0\} & \{0\} & \{0\} \\ [0] & k_1b_1^2+k_2b_2^2 & k_1b_1-k_2b_2 & -k_1b_1 & k_2b_2 & 0 & 0 \\ [0] & k_1b_1-k_2b_2 & k_1+k_2 & -k_1 & -k_2 & 0 & 0 \\ -k_3[\mathbf{N}_1]-c_3[\mathbf{N}_1]_x\dot{\mathbf{x}}_1 & -k_1b_1 & -k_1 & k_1+k_3 & 0 & 0 & 0 \\ -k_4[\mathbf{N}_2]-c_4[\mathbf{N}_2]_x\dot{\mathbf{x}}_2 & k_2b_2 & -k_2 & 0 & k_2+k_4 & 0 & 0 \\ [0] & 0 & 0 & 0 & 0 & k_{t1} & -k_{t1} \\ -k_{t2}[\mathbf{N}_3]-c_{t2}[\mathbf{N}_3]_x\dot{\mathbf{x}}_3 & 0 & 0 & 0 & 0 & -k_{t1} & k_{t1}+k_{t2} \end{bmatrix} \tag{16}$$

$$\{\boldsymbol{F}\}=\begin{pmatrix} \sum_{i=0}^{3}[\mathbf{N}_i]^T \hat{\boldsymbol{f}}_i \\ 0 \\ 0 \\ k_3r(x_1)+c_3r'(x_1)\boldsymbol{v} \\ k_4r(x_2)+c_4r'(x_2)\boldsymbol{v} \\ 0 \\ k_{t2}r(x_3)+c_{t2}r'(x_3)\boldsymbol{v} \end{pmatrix} \tag{17}$$

where in the Eqn. (14) and (17):

$$\boldsymbol{f}_{\theta 1}=\frac{1}{b_1+b_2}I_0,\quad \boldsymbol{f}_{\theta 2}=-\frac{1}{b_1+b_2}I_0 \tag{18}$$

$$\begin{aligned}
\hat{\boldsymbol{f}}_1&=-\frac{b_2}{b_1+b_2}m_0\boldsymbol{g}-m_1\boldsymbol{g}+k_3r(x_1)+c_3r'(x_1)\boldsymbol{v},\\
\hat{\boldsymbol{f}}_2&=-\frac{b_1}{b_1+b_2}m_0\boldsymbol{g}-m_2\boldsymbol{g}+k_4r(x_2)+c_4r'(x_2)\boldsymbol{v},\\
\hat{\boldsymbol{f}}_3&=-m_{t0}\boldsymbol{g}-m_{t1}\boldsymbol{g}+k_{t2}r(x_3)+c_{t2}r'(x_3)\boldsymbol{v}
\end{aligned} \tag{19}$$

and $\boldsymbol{f}_{\theta 1}$ and $\boldsymbol{f}_{\theta 2}$ are forces due to the moment of rotational inertia of the tractor. $\hat{\boldsymbol{f}}_1$, $\hat{\boldsymbol{f}}_2$ and $\hat{\boldsymbol{f}}_3$ are forces due to the inertia of tractor and trailer axles. In the Eqns. (14), (15) and (16) the sub-matrices [$\mathbf{M}_b$] and [$\mathbf{K}_b$] are obtained from [67]. The Rayleigh type of damping considered for the beam is defined as follows:

$$[\mathbf{C}_b]=\alpha[\mathbf{M}_b]+\beta[\mathbf{K}_b] \tag{20}$$

α and β are calculated according to the following relations:

$$\alpha=-\frac{2\omega_1\omega_2(\xi_1\omega_2-\xi_2\omega_1)}{\omega_2^2-\omega_1^2} \tag{21}$$

$$\beta=-\frac{2(\xi_2\omega_2-\xi_1\omega_1)}{\omega_2^2-\omega_1^2}, \tag{22}$$

the first and second frequencies of the beam are given by ω_1 and ω_2, respectively [67].

Modal analysis method

In this section, TT and bridge interaction equations needed for the modal analysis are derived. TT vibration equation is represented in Eqn. (3). Vehicle-bridge interaction relationships in the modal analysis are derived using the relations described in [68], which were for train-bridge interaction. Modified relationships have been derived for the case of TT passing a bridge. The bridge vibration due to the moving TT is given as:

$$[\mathbf{M}_b]\{\ddot{\boldsymbol{w}}\}+[\mathbf{C}_b]\{\dot{\boldsymbol{w}}\}+[\mathbf{K}_b]\{\boldsymbol{w}\}=\sum_{k=1}^{n_f}\delta\{\boldsymbol{F}_{bk}\} \tag{23}$$

where, [$\mathbf{M}_b$], [$\mathbf{C}_b$], and [$\mathbf{K}_b$] represent the mass, stiffness, and damping of the beam, n_f is the number of contact points of the TT with the bridge, δ denotes the Dirac delta function, and $\boldsymbol{w}$ is the vertical displacement of the beam. The contact points x_1, x_2, and x_3, which are shown in Fig. 4b, denote the TT contact points from the beginning of the beam; they are expressed as:

$$x_1=\boldsymbol{v}t+b_3,\quad x_2=\boldsymbol{v}t+(b_1+b_2+b_3),\quad x_3=\boldsymbol{v}t \tag{24}$$

$$\boldsymbol{F}_{bk}=\boldsymbol{R}_{wk}-\boldsymbol{F}_{wk} \tag{25}$$

In the above equation, $\boldsymbol{F}_{bk}$ represents the forces that apply to the beam by the TT, and $\boldsymbol{F}_{bk}$ consists of two forces of weight ($\boldsymbol{R}_{wk}$) and the force of inertia ($\boldsymbol{F}_{wk}$) applied by the TT.

$$\boldsymbol{R}_{w1}=\left[m_0\left(\frac{b_2}{b_1+b_2}\right)+m_1\right]\boldsymbol{g} \tag{26}$$

$$\boldsymbol{R}_{w2}=\left[m_0\left(\frac{b_1}{b_1+b_2}\right)+m_2\right]\boldsymbol{g} \tag{27}$$

$$\boldsymbol{R}_{w3}=(m_{t0}+m_{t1})\boldsymbol{g} \tag{28}$$

$$\boldsymbol{F}_{w1}=m_1\ddot{\boldsymbol{d}}_3+\frac{I_0\ddot{\boldsymbol{d}}_1+m_0b_1\ddot{\boldsymbol{d}}_2}{b_1+b_2} \tag{29}$$

$$\boldsymbol{F}_{w2}=m_2\ddot{\boldsymbol{d}}_4+\frac{I_0\ddot{\boldsymbol{d}}_1+m_0b_2\ddot{\boldsymbol{d}}_2}{b_1+b_2} \tag{30}$$

$$\boldsymbol{F}_{w3}=m_{t1}\ddot{\boldsymbol{d}}_6+m_{t0}\ddot{\boldsymbol{d}}_5 \tag{31}$$

Based on modal superposition and separation of variables, beam displacement can be represented as:

$$\boldsymbol{w}(x,t)=\sum_{j=1}^{n}\boldsymbol{\phi}_j(x)q_j(x) \tag{32}$$

where $\{q_j(t), j=1,2,..,n\}$ are the generalized coordinates, and n is the number of vibration modes. Vibration modes are considered to be of the form of solution a simply supported beam:

$$\phi_j=\sin\left(\frac{j\pi x}{L}\right) \tag{33}$$

Combination of Eqns. (3) and (23) yield an interaction relation that contains modal components of the beam and physical components of the TT:

$$\begin{bmatrix}\mathbf{M}_{bb} & 0\\ 0 & \mathbf{M}_v\end{bmatrix}\begin{pmatrix}\ddot{\boldsymbol{q}}\\ \ddot{\boldsymbol{d}}\end{pmatrix}+\begin{bmatrix}\mathbf{C}_{bb} & -\frac{2\mathbf{c}_{sk}}{m_lL}\boldsymbol{\Phi}^T\\ -\mathbf{c}_{sk}\boldsymbol{\Phi} & \mathbf{C}_v\end{bmatrix}\begin{pmatrix}\dot{\boldsymbol{q}}\\ \dot{\boldsymbol{d}}\end{pmatrix}+\begin{bmatrix}\boldsymbol{K}_{bb} & -\frac{2\mathbf{k}_{sk}}{m_lL}\boldsymbol{\Phi}^T\\ \mathbf{k}_{sk}\boldsymbol{\Phi}-v\mathbf{c}_{sk}\boldsymbol{\Phi}' & \boldsymbol{K}_v\end{bmatrix}\begin{pmatrix}\boldsymbol{q}\\ \boldsymbol{d}\end{pmatrix}=\begin{pmatrix}\boldsymbol{F}_{bb}\\ \boldsymbol{F}_{vv}\end{pmatrix} \tag{34}$$

where, [$\mathbf{M}_{bb}$], [$\mathbf{C}_{bb}$], and [$\mathbf{K}_{bb}$] are the mass, damping, and stiffness matrices of the beam, respectively. In the aforementioned equations, $\boldsymbol{F}_{bb}$ represents the forces that act on the beam due to TT, and $\boldsymbol{F}_{vv}$ shows the forces that act on TT due to the beam vibrations. The sub-matrices of the above system are defined as follows [68,69]:

$$\mathbf{M}_{bb}=[\mathbf{I}] \tag{35}$$

$$0\,\mathbf{C}_{bb}=diag[2\zeta_j\omega_j]+\frac{2}{m_lL}\sum_{k=1}^{n_f}(\boldsymbol{\phi}_k\mathbf{c}_{sk}\boldsymbol{\phi}_k^T) \tag{36}$$

$$\mathbf{K}_{bb} = diag[\omega_j^2] + \frac{2}{m_l L}\sum_{k=1}^{n_f}(v\boldsymbol{\phi}_k \mathbf{c}_{sk}\boldsymbol{\phi}_k^{'} + \boldsymbol{\phi}_k \mathbf{k}_{sk}\boldsymbol{\phi}_k^{T}) \tag{37}$$

$$\boldsymbol{F}_{bb} = -\frac{2}{m_l L}\sum_{k=1}^{n_f}(\boldsymbol{R}_{wk} + v c_{sk} r_k^{'} + k_{sk} r_k)\boldsymbol{\phi}_k^{T} \tag{38}$$

$$\boldsymbol{F}_{vv} = \begin{Bmatrix} 0 \\ 0 \\ v c_3 r_1^{'} + k_3 r_1 \\ v c_4 r_2^{'} + k_4 r_2 \\ 0 \\ v c_{t2} r_3^{'} + k_{t2} r_3 \end{Bmatrix} \tag{39}$$

$$\boldsymbol{\phi}_k = \begin{Bmatrix} \phi_1(x_k) & \phi_2(x_k) & \cdots & \phi_n(x_k) \end{Bmatrix}^T \tag{40}$$

$$\boldsymbol{\Phi} = \begin{bmatrix} \phi_1(x_1) & \phi_1(x_2) & \phi_1(x_3) \\ \phi_2(x_1) & \phi_2(x_2) & \phi_2(x_3) \\ \vdots & \vdots & \vdots \\ \phi_n(x_1) & \phi_n(x_2) & \phi_n(x_3) \end{bmatrix} \tag{41}$$

$$\mathbf{c}_{sk} = \begin{bmatrix} 0 & 0 & 0 \\ 0 & 0 & 0 \\ c_3 & 0 & 0 \\ 0 & c_4 & 0 \\ 0 & 0 & 0 \\ 0 & 0 & c_{t2} \end{bmatrix}, \quad \mathbf{k}_{sk} = \begin{bmatrix} 0 & 0 & 0 \\ 0 & 0 & 0 \\ k_3 & 0 & 0 \\ 0 & k_4 & 0 \\ 0 & 0 & 0 \\ 0 & 0 & k_{t2} \end{bmatrix}, \tag{42}$$

In the above equations, m_l, E, I, ω_j, and ζ_j are the per-unit-length mass, modulus of elasticity, the flexural moment of inertia, the jth undamped natural frequency, and damping ratio, respectively. $\mathbf{M}_v$, $\mathbf{C}_v$ and $\mathbf{K}_v$ are the vehicle matrices in Eqn. (3). The natural frequency of the beam is given as:

$$\omega_j = \left(\frac{j\pi}{L}\right)^2 \sqrt{\frac{EI}{m_l}} \tag{43}$$

The TT vibration is then achieved from both methods by implementing the parameters specified in Tab. 1 for beam and TT. Two approaches were used to determine the vertical displacement of the trailer (d_5) at different speeds (see Fig. 5a). A comparison of modal and finite element results is made to explore the influence of the number of elements on the accuracy of the FEM results, where 30 vibration modes are evaluated in the case of modal analysis (see Fig. 5b). It should be noted that when the front axle reaches the end of the beam, the TT stops moving.

Parameter	value	Parameter	value	Parameter	value	Parameter	value	Parameter	value
I_0	172160	k_1	1969034	c_1	7181.8	b_1	3	E	2.1×10^{11}
m_0	12404	k_2	727812	c_2	2189.6	b_2	3	ζ	0.01
m_1	725.4	k_3	4735000	c_3	0	b_3	2		
m_2	725.4	k_4	1972900	c_4	0	ρ	7855		
m_{t0}	5000	k_{t1}	100000	c_{t1}	0	L	60		
m_{t1}	2000	k_{t2}	300000	c_{t2}	0	I	0.6667		

Table 1: Parameters of the TT, and of the bridge (Mass moment of inertia is in $kg.m^2$, mass is in kg, stiffness is in N/m, damping is in $N.s/m$, length is in m, Young's modulus is in N/m^2, moment of inertia is in m^4, and specific mass is in kg/m^3).

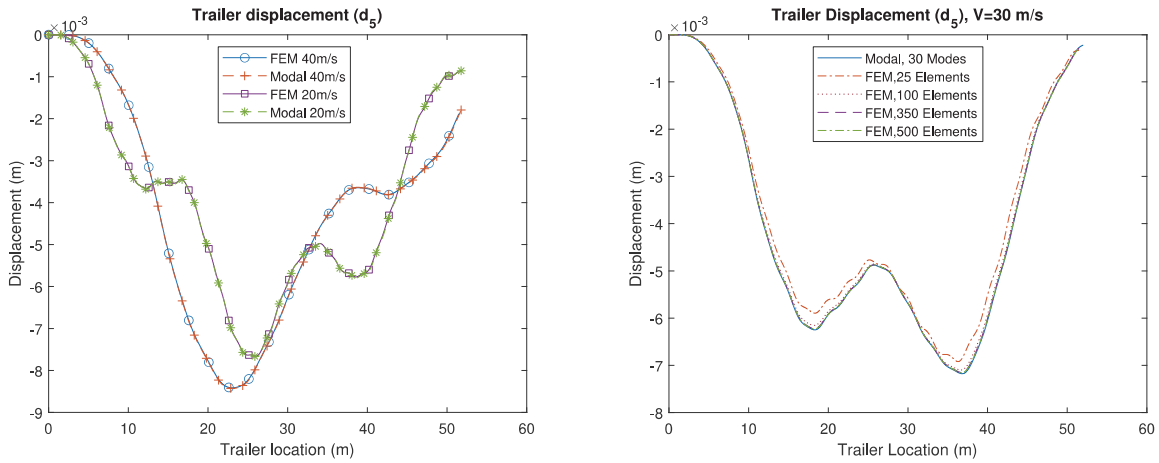

(a) (b)

Figure 5: (a) Trailer vertical displacement in FEM and modal analysis, (b) Comparing 30 modes in modal with 25, 100, 350, and 500 elements in FEM.

Damaged element

In order to represent damage, the stiffness matrix of the damaged element is needed, the damaged element with crack depth a is shown in Fig. 6. For an arbitrary load in the absence of shear deformation, the strain energy of the beam element without crack is defined as [70]:

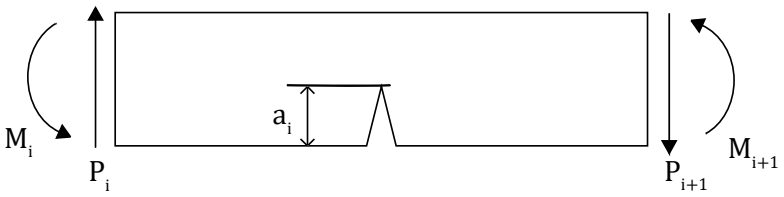

Figure 6: Damaged element with crack of depth a.

$$W^0 = \frac{1}{2EI}\left(\boldsymbol{M}^2 l + \boldsymbol{MP} l^2 + \frac{\boldsymbol{P}^2 l^3}{3}\right) \tag{44}$$

where in the above equation, P and M are the shear force and bending moment applied to the element and l is the length of the element. Additional energy as a result of crack presence can be obtained from Castigliano's theorem. For a rectangular cross-section beam with height h, width b, the excess energy from the crack is written as:

$$W^{(1)} = b\int_0^a \left(\frac{K_I^2 + K_{II}^2}{E'} + \frac{(1+\upsilon)K_{III}^2}{E} \right) da \tag{45}$$

where $E' = E$ in case of plane stress, for plane strain $E' = E/(1-\upsilon^2)$, and a is the crack depth. The stress intensity factors of modes I, II, and III are represented by K_I, K_{II}, and K_{III}, respectively. Writing the excess energy due to the presence of a crack and neglecting axial force, will read as [71]:

$$W^{(1)} = b\int_0^a \left(\frac{(K_{IM} + K_{IP})^2 + K_{IIP}^2}{E'} \right) da \tag{46}$$

$$K_{IM} = \frac{6\boldsymbol{M}\sqrt{\pi a}\boldsymbol{F}_I(s)}{bh^2}, \quad K_{IP} = \frac{3\boldsymbol{P}l\sqrt{\pi a}\boldsymbol{F}_I(s)}{bh^2}, \quad K_{IIP} = \frac{\boldsymbol{P}\sqrt{\pi a}\boldsymbol{F}_{II}(s)}{bh} \tag{47}$$

$$\begin{aligned} \boldsymbol{F}_I(s) &= \sqrt{\frac{2}{\pi s}\tan\left(\frac{\pi s}{2}\right)}\frac{0.923 + 0.199[1-\sin \pi s/2]^4}{\cos \pi s/s}, \\ \boldsymbol{F}_{II}(s) &= (3s - 2s^2)\frac{1.122 + -0.561s + 0.085s^2 + 0.18s^3}{\sqrt{1-s}} \end{aligned} \tag{48}$$

In the above equations, s is the ratio of crack depth to beam depth. The flexibility matrix of an intact element is expressed as:

$$\mathbf{c}_{ij}^{(0)} = \frac{\partial \boldsymbol{u}^2 W^{(0)}}{\partial \boldsymbol{P}_i \partial \boldsymbol{P}_j}, \quad i,j = 1,2, \quad \boldsymbol{P}_1 = \boldsymbol{P}, \quad \boldsymbol{P}_2 = \boldsymbol{M} \tag{49}$$

The coefficient of additional flexibility due to the presence of cracks is defined as follows:

$$\tilde{\mathbf{c}}_{ij}^{(1)} = \frac{\partial \boldsymbol{u}^2 W^{(1)}}{\partial \boldsymbol{P}_i \partial \boldsymbol{P}_j}, \quad i,j = 1,2, \quad \boldsymbol{P}_1 = \boldsymbol{P}, \quad \boldsymbol{P}_2 = \boldsymbol{M} \tag{50}$$

Finally, the total flexibility will read as,

$$\tilde{\mathbf{c}}_{ij} = \tilde{\mathbf{c}}_{ij}^{(0)} + \tilde{\mathbf{c}}_{ij}^{(1)} \tag{51}$$

The equilibrium conditions are described as follows:

$$\begin{pmatrix} \boldsymbol{P}_i & \boldsymbol{M}_i & \boldsymbol{P}_{i+1} & \boldsymbol{M}_{i+1} \end{pmatrix}^T = [\mathbf{T}]\begin{pmatrix} \boldsymbol{P}_{i+1} & \boldsymbol{M}_{i+1} \end{pmatrix} \tag{52}$$

$$[\mathbf{T}] = \begin{pmatrix} -1 & -L & 1 & 0 \\ 0 & -1 & 0 & 1 \end{pmatrix}^T \tag{53}$$

According to the principle of virtual work, the stiffness matrix of the damaged element can be reached as [37,71]:

$$[\mathbf{K}]_e = [\mathbf{T}]^T[\tilde{\mathbf{c}}][\mathbf{T}] \tag{54}$$

This stiffness matrix is used in the FE model of the bridge to represent the damaged locations. Damaged beam frequencies are compared to laboratory data [72] to confirm the accuracy of finite element modeling results for a cracked beam. A steel cantilever beam with Young's modulus of 206 *GPa*, width and height of 20 *mm*, Length of 300 *mm*, and specific mass of 7750 kg/m^3 is considered. The beam's first and second frequencies resulted in the FE model and experimental data [72] are given for various crack depths and locations in Tab. 2. These results clearly demonstrate the of accuracy of the developed FE code in predicting damaged beam frequencies.

Crack location	Crack depth	Method	Natural Frequency		Error (%)	
			1st	2nd	1st	2nd
Intact	-	Exp [72]	185.2	1160.6	-	-
		FEM	185.1	1159.9	0.05	0.06
80	2	Exp [72]	184	1160	-	-
		FEM	184	1159.2	0	0.07
80	6	Exp [72]	174.7	1155.3	-	-
		FEM	176.4	1154.5	-0.9	0.07
140	2	Exp [72]	184.7	1153.1	-	-
		FEM	184.7	1152.1	0	0.09
140	6	Exp [72]	181.2	1092.9	-	-
		FEM	181.9	1098.1	-0.4	0.5

Table 2: Comparisons between the first two natural frequencies derived from FEM, and the experimental study (length is in *mm* and frequency is in *Hz*).

The deviations observed in Tab. 2 between the experimental data and the FEM results are relatively small, indicating that the FE model is quite accurate in predicting the natural frequencies of the damaged beam. The discrepancies can be attributed to several factors, including potential variations in material properties, slight differences in the actual versus modeled crack sizes, and inherent experimental measurement errors. Specifically, the minor errors in the 1st and 2nd natural frequencies, ranging from 0 to 0.9%, reflect the model's robustness. The slightly larger deviation at the 6 mm crack depth and 140 mm location (0.5% in the 2nd frequency) suggests that as crack depth increases, the complexity of accurately modeling the damage also increases, leading to higher deviations. This reinforces the importance of ongoing refinement of the FE model to account for such complexities in real-world applications.

Road surface profiles

Vehicle responses can be significantly affected by the road surface's roughness. Probability characterizes surface roughness, according to ISO 8608 [73]. The surface roughness quality can be provided by power spectral density (PSD) according to the following equation:

$$G_d(n) = G_d(n_0)\left(\frac{n}{n_0}\right)^{-w} \tag{55}$$

where n is the spatial frequency per meter, w=2, and n_0=0.1 *cycles/m*. Surface quality can be classified into eight grades based on the roughness height. In this categorization, *A* stands for the best surface level and *H* is the worst. For classes A, B and C, the value 0.1×10^{-6} (m^3), 128×10^{-6} (m^3) and 512×10^{-6} (m^3) are assumed for $G_d(n_0)$, respectively [74]. The amplitude of surface irregularities is shown as:

$$d = \sqrt{2G_d(n)\Delta n} \tag{56}$$

where Δn represents spatial frequency sampling. Finally, the relationship between surface irregularities is defined as follows:

$$r(x)=\sum(d_i cos(n_i x+\theta_i)) \tag{57}$$

In this relation, n_i is the ith spatial frequency, d_i is the surface irregularity amplitude, and θ_i is the random phase angle, which here is a uniform distribution within the range [0,2π) [46]. Three classes A, B, and C, are considered here as representatives of rough road profiles (see Fig. 7).

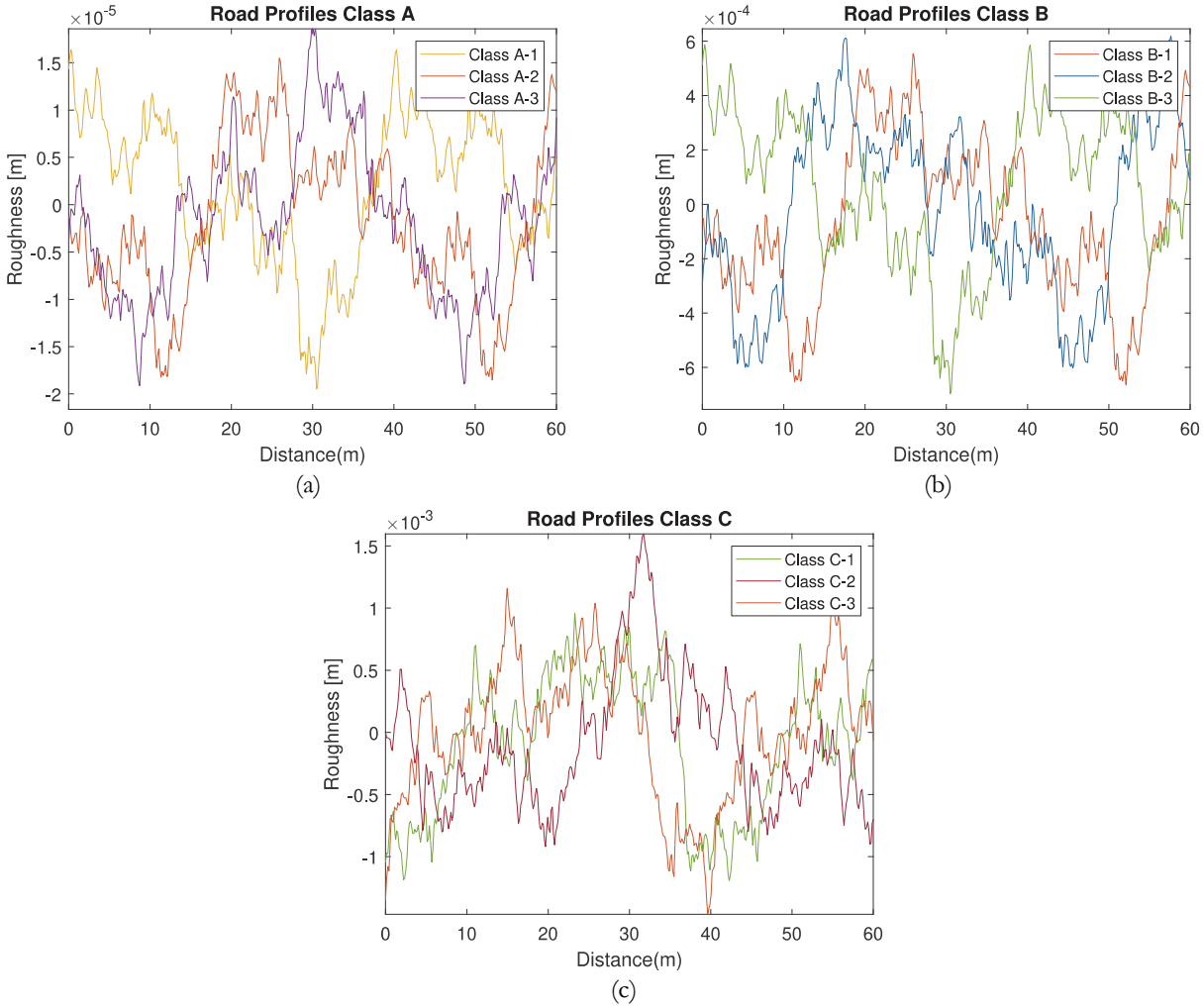

Figure 7: (a) Road profile class A, (b) Road profile class B, (c) Road profile class C

Vibration signal

Laser sensors can be used to detect relative acceleration between the beam and the trailer axle (see Fig. 8). The beam acceleration below the trailer axle is calculated by subtracting this relative acceleration from the absolute acceleration of the trailer axle, which read as:

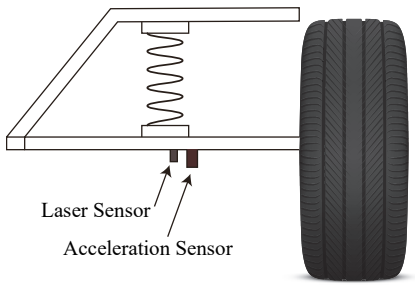

Figure 8: Sensors mounted on the trailer axle.

$$\ddot{\boldsymbol{Y}}_{tt} = \ddot{\boldsymbol{Y}}_{t} - \ddot{\boldsymbol{Y}}_{r}, \tag{58}$$

where, $\ddot{\boldsymbol{Y}}_{tt}$, $\ddot{\boldsymbol{Y}}_{t}$, and $\ddot{\boldsymbol{Y}}_{r}$ represent beam acceleration under the trailer axle, absolute acceleration of trailer axle, and relative acceleration between trailer axle and beam, respectively. An illustration of these parameters is given in Fig. 9. The beam acceleration under the trailer axle is analyzed through both the EMD and VMD in the following bridge damage scenarios.

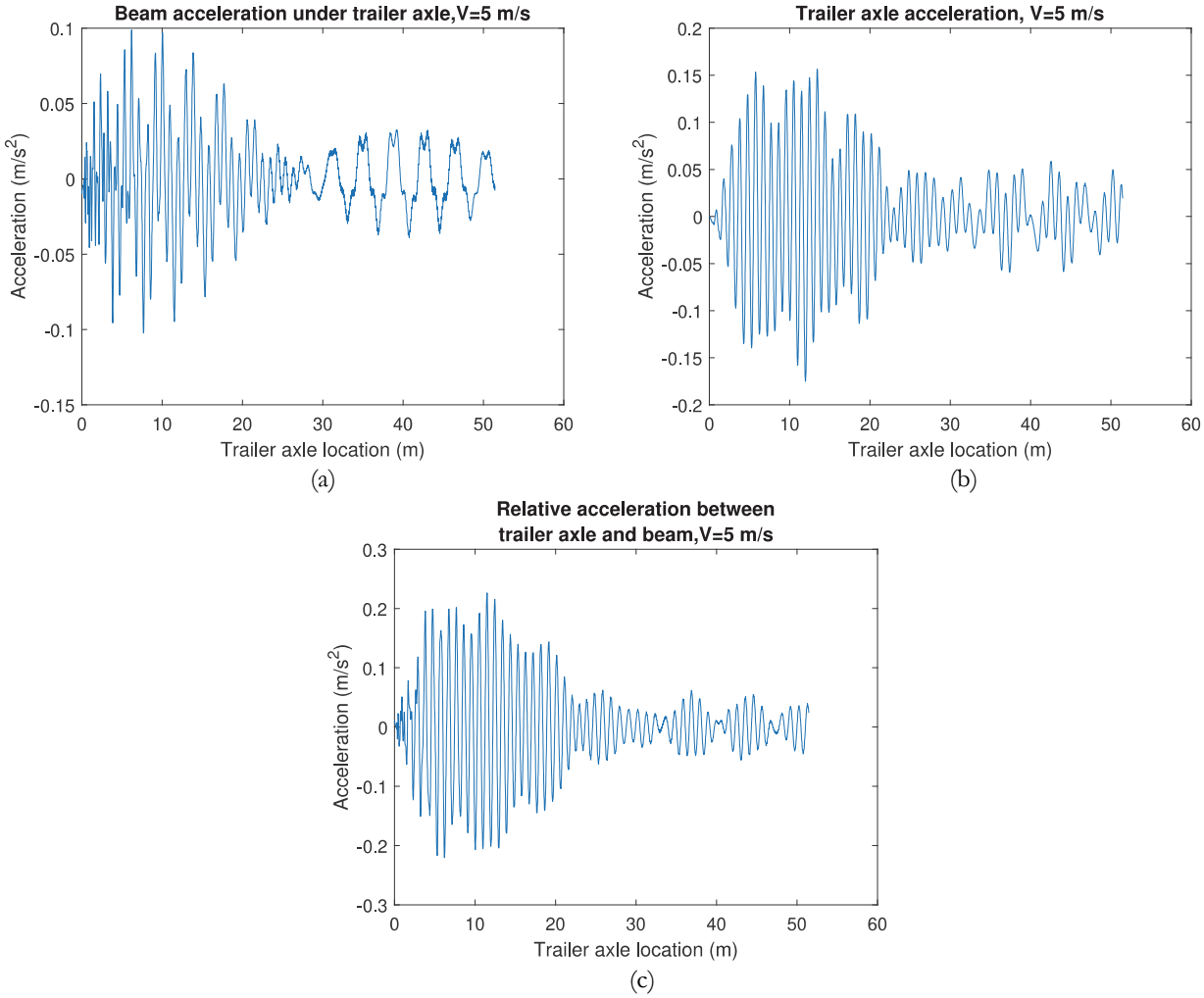

Figure 9: (a) Beam acceleration under trailer axle, (b) Absolute trailer axle acceleration, (c) Relative acceleration between trailer axle and beam.

RESULTS AND DISCUSSIONS

In order to investigate the applicability of the proposed methodology in identifying damages, different damage scenarios are examined according to Tab. 3. All signals are collected at 5 m/sec velocity.

EMD was used to analyze damage scenarios (P2, A2, B2, C2) to find the location of damages. The number of modes extracted by EMD is 7 modes in the P1, B2, and C2 scenarios, and 8 modes in the A2 scenario. The location of the damage is not evident in any of the instantaneous energy diagrams, as shown in Fig. 10. The VMD approach's performance to spot damage will be described further below.

Road Class	Damage Case	Location	Severity
Class Perfect	P1	L/3	10%
	P2	L/2	10%
	P3	2L/3	10%
Class A	A1	L/3	10%
	A2	L/2	10%
	A3	2L/3	10%
Class B	B1	L/3	20%
	B2	L/2	20%
	B3	2L/3	20%
Class C	C1	L/3	20%
	C2	L/2	20%
	C3	2L/3	20%

Table 3: All Damage scenarios with road classes, locations, and severity.

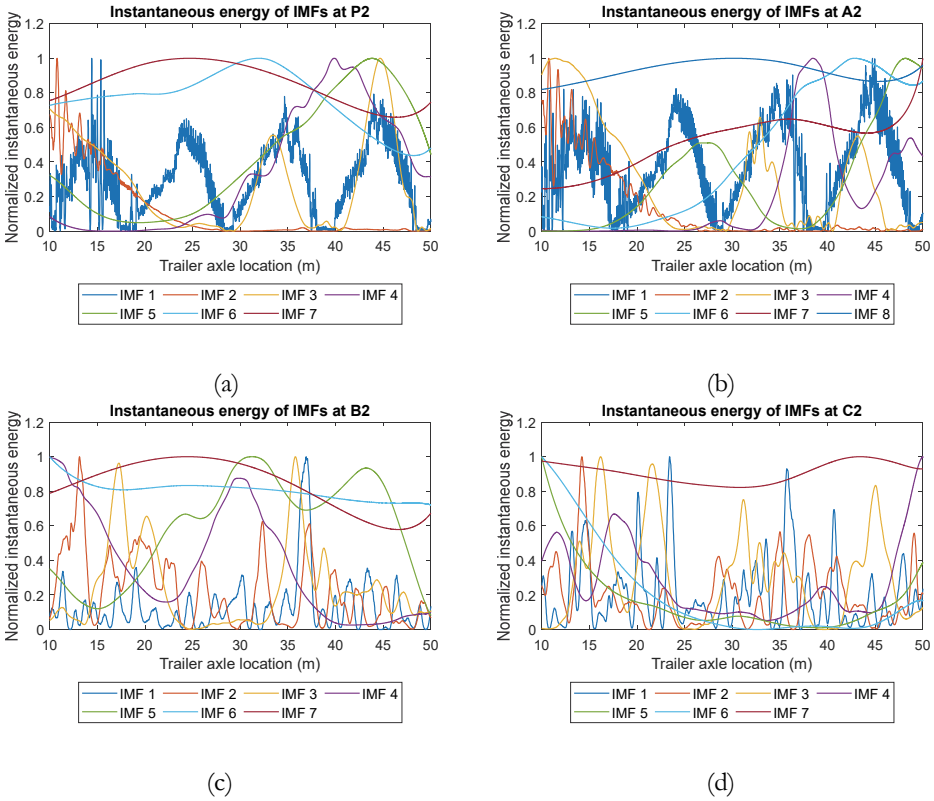

Figure 10: Normalized instantaneous energy of IMFs extracted through EMD for cases (a) P2, (b) A2, (c) B2, (d) C2.

To capture the effects of imposing damage to the bridge, the output signal's frequency spectrum is evaluated. Scrutiny of the spectrum reveals that there is a notable difference between the intact and damaged cases. This difference is evident within the frequency range 0.01-0.15 Hz, as shown in Fig. 11. By decomposing the signal with VMD, in IMFs with central frequencies around 0.06 and 0.07~Hz damage can be seen as a peak in the corresponding IMF energy signal. In each case, the given signal is decomposed into 40 IMFs. The normalized instantaneous energy for P1, P2, and P3 damage is shown in Fig. 12, in this figure, the damage can be detected at the peak of the diagrams when compared to the intact case. Several normalized instantaneous energies of IMFs at P1 damage are shown in Fig. 13. The site of the damage is evident in these IMFs, as can be observed. In the following, just one IMF is utilized, where the damage is most visible.

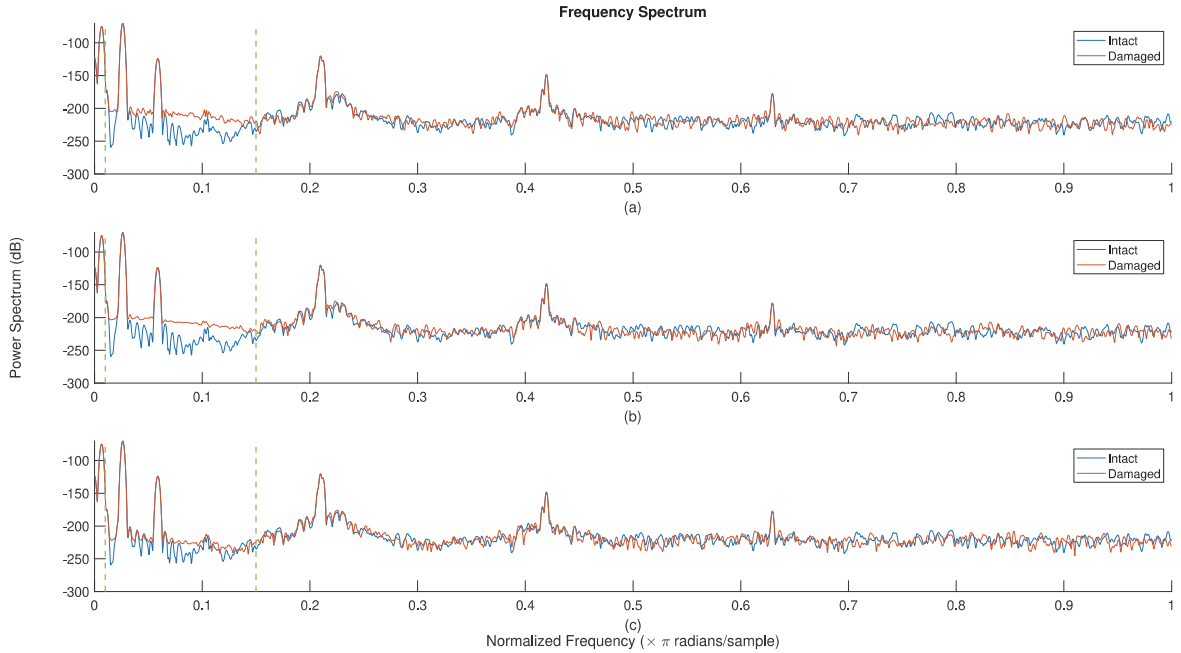

Figure 11: Frequency spectrum for cases (a) P1, (b) P2, (c) P3.

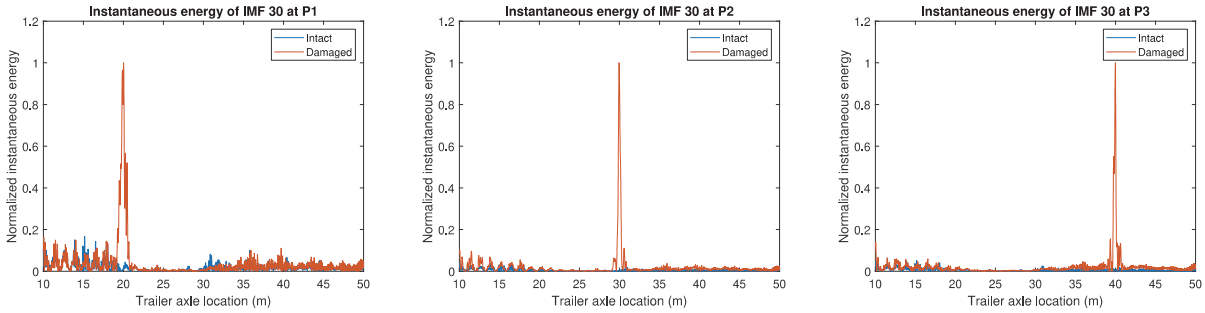

Figure 12: Normalized instantaneous energy of IMF extracted through VMD for cases (a) P1, (b) P2, (c) P3.

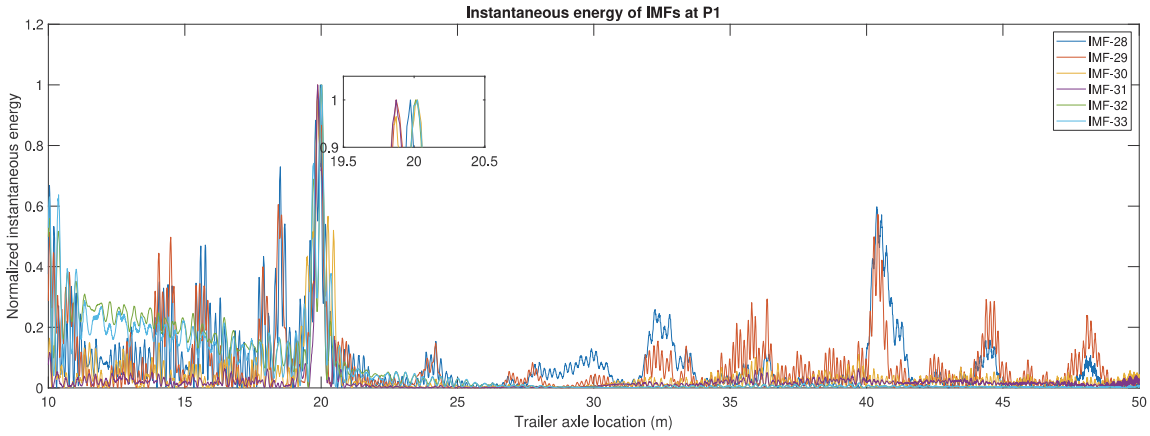

Figure 13: Normalized instantaneous energy of IMFs extracted through VMD for P1 Damage scenario with six IMFs.

In order to determine the damage in other cases, their frequency spectrum is shown (see Appendix B), and the instantaneous energy of the related IMFs is extracted in those central frequencies based on the significant difference between the intact and damaged cases (see Fig. 14).

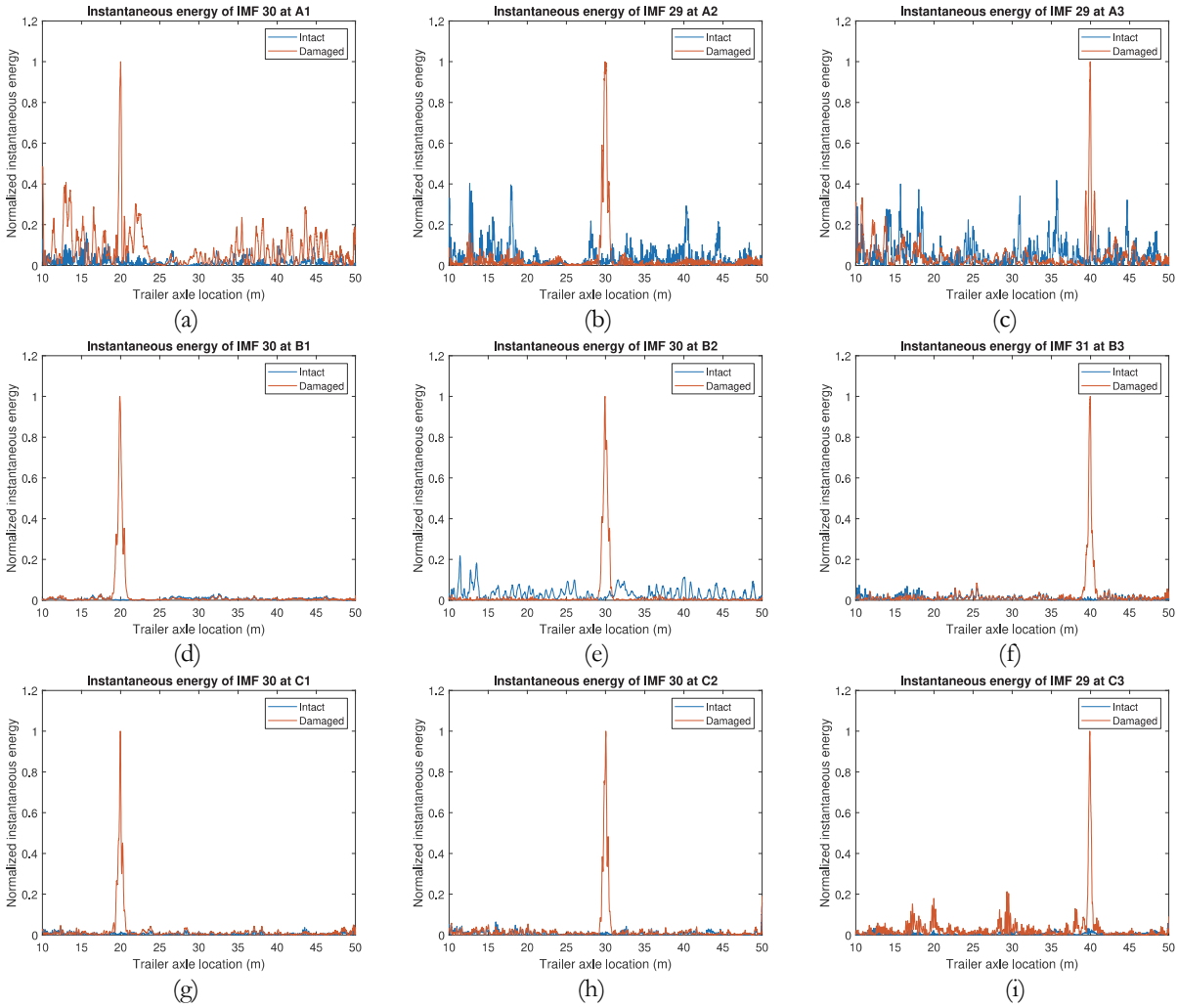

Figure 14: Normalized instantaneous energy of IMF extracted through VMD for cases (a) A1, (b) A2, (c) A3, (d) B1, (e) B2, (f) B3, (g) C1, (h) C2, (i) C3.

The use of VMD and instantaneous energy from IMFs show that this technique is capable of detecting anomalies in vehicle acceleration signals caused by damage. Fig. 15 provides an analysis of the effect of minor damage in Class B and Class C irregularities. It is worth noting that in both Class B and Class C, 10% of the damage is undetectable. While peaks are visible in certain scenarios, such as B2 and C2, these anomalies are not consistently observable. The corresponding damage scenarios are summarized in Tab. 4.

Road Class	Damage Case	Location	Severity
Class B	$B1_{ls}$	L/3	10%
	$B2_{ls}$	L/2	10%
	$B3_{ls}$	2L/3	10%
Class C	$C1_{ls}$	L/3	10%
	$C2_{ls}$	L/2	10%
	$C3_{ls}$	2L/3	10%

Table 4: Less severe damage cases in road classes B and C.

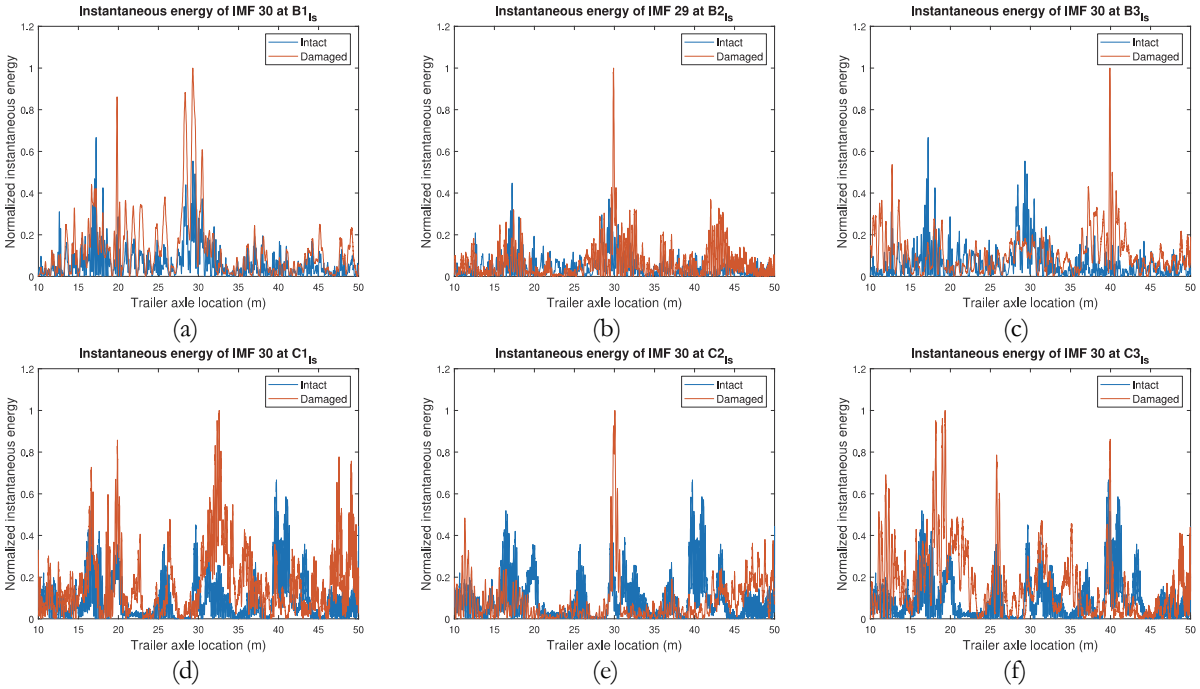

Figure 15: Normalized instantaneous energy of IMF extracted through VMD for cases (a) $B1_{ls}$, (b) $B2_{ls}$, (c) $B3_{ls}$, (d) $C1_{ls}$, (e) $C2_{ls}$, (f) $C3_{ls}$.

Effect of velocity

In this section, the effects of various TT speed on damage detection are investigated. It is evident from the simulation results that the damage location can be determined at varied speeds. This is illustrated in Fig 16. The normalized instantaneous energy of A2, B2, and C2 damage scenarios is shown in this figure. Different velocities ranging from 2 *m/sec* to 30 *m/sec* are investigated. The noise in the IMF's normalized instantaneous energy is more pronounced at low speeds, e.g. for 2 *m/sec* than the higher speeds.

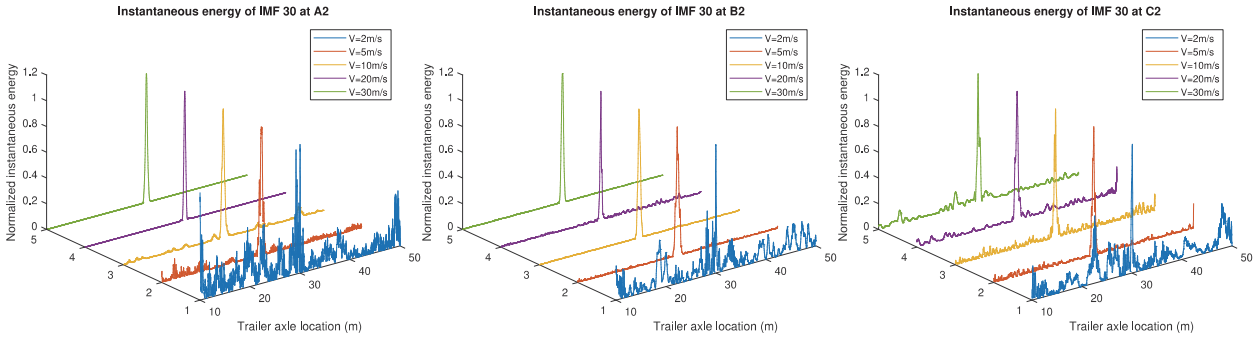

Figure 16: Normalized instantaneous energy at different velocities extracted through VMD for cases (a) A2, (b) B2, (c) C2.

Based on the simulation results, the VMD method is effective in detecting damages across a wide range of vehicle speeds. Specifically, within the range of 2 *m/sec* to 30 *m/sec*, damage detection remains reliable. This demonstrates the robustness of the VMD approach in varying operational conditions. However, at the lower end of this speed range, increased noise levels can introduce more fluctuations in the normalized instantaneous energy, although damage locations are still discernible.

Effect of mass ratio

The examination of damage detection under various trailer masses is also examined. Tab. 5. illustrates the different masses associated with m_{t0} and m_{t1} in different cases. Fig. 17 displays the impacts of mass when the TT passes through the A2 damage scenario.

Mass Cases	Trailer Mass
MR1	m_{t0}=875 m_{t1}=62.5
MR2	m_{t0}=1750 m_{t1}=125
MR3	m_{t0}=3500 m_{t1}=250
MR4	m_{t0}=7000 m_{t1}=500
MR5	m_{t0}=14000 m_{t1}=1000

Table 5: Various trailer masses (mass is in *kg*).

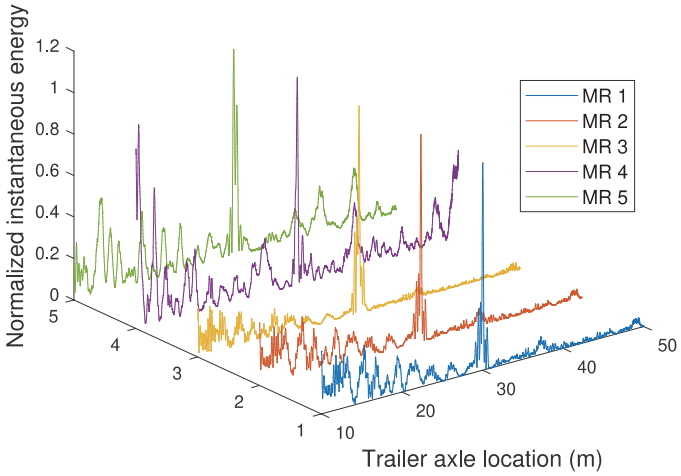

Figure 17: Normalized instantaneous energy at different trailer mass ratios extracted through VMD for A2 damage scenario.

Effect of noise

The ambient noise is present while measuring acceleration and displacement sensors, and will affect the method accuracy. Thus, the impact of noise levels on damage detection has been studied in this section. Starting with the equation of noise which is given as:

$$\boldsymbol{S}n = \boldsymbol{S} + \alpha \boldsymbol{N} \tag{59}$$

where $\boldsymbol{S}n$ is a noisy signal, $\boldsymbol{S}$ is a clean signal, $\boldsymbol{N}$ is a random vector with a normal distribution, and α is a coefficient for applying noise with the desired signal-to-noise ratio (SNR). To suppress the inconsistency emanating from the presence of noise, the results of passing vehicle ten times are recorded and averaged. The applied noise with SNR of 40 *dB* is added to the signals which is shown in Fig. 18.

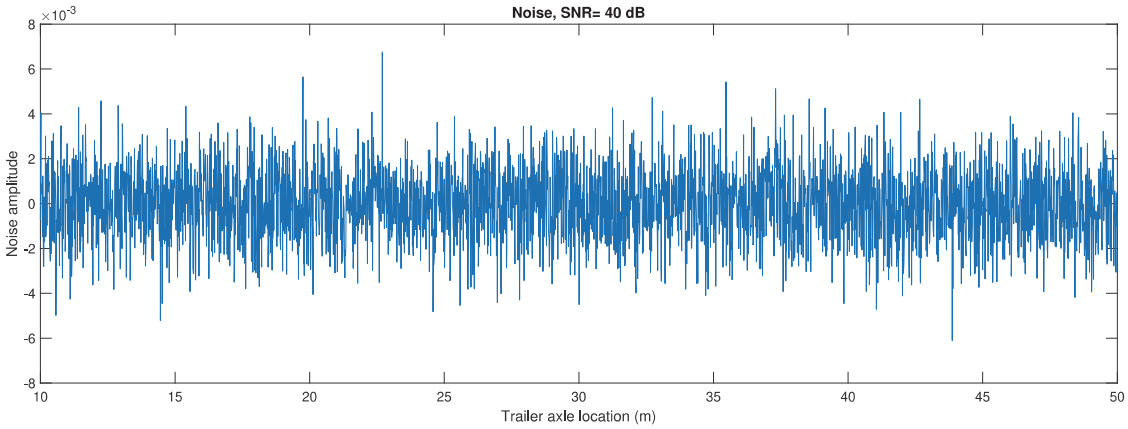

Figure 18: Noise with SNR=40 *dB*.

The normalized instantaneous energy of the IMFs related to P1, P2, and P3 Damages is shown in Fig. 19a-c. As it is evident, the peaks of diagrams can still be used to illustrate the location of the damage, approving that the noise effect can be handled effectively by the VMD. A1, A2, and A3 damages with noise impact are visualized in Fig. 19d-f, although the noise has caused fluctuations in the normalized instantaneous energy diagram, the location of the damage is still easily recognizable. The demonstration of the noise effect in B1, B2, and B3 is shown in Fig. 19g-i, the peaks in the figure clearly illustrate where the damages occurred. Signals in C1, C2, and C3 are affected by noise as seen in Fig. 19j-l. As indicated in the figure, there were several peaks in the diagrams, but these peaks do not even reach half of the highest peak at the location of damages.

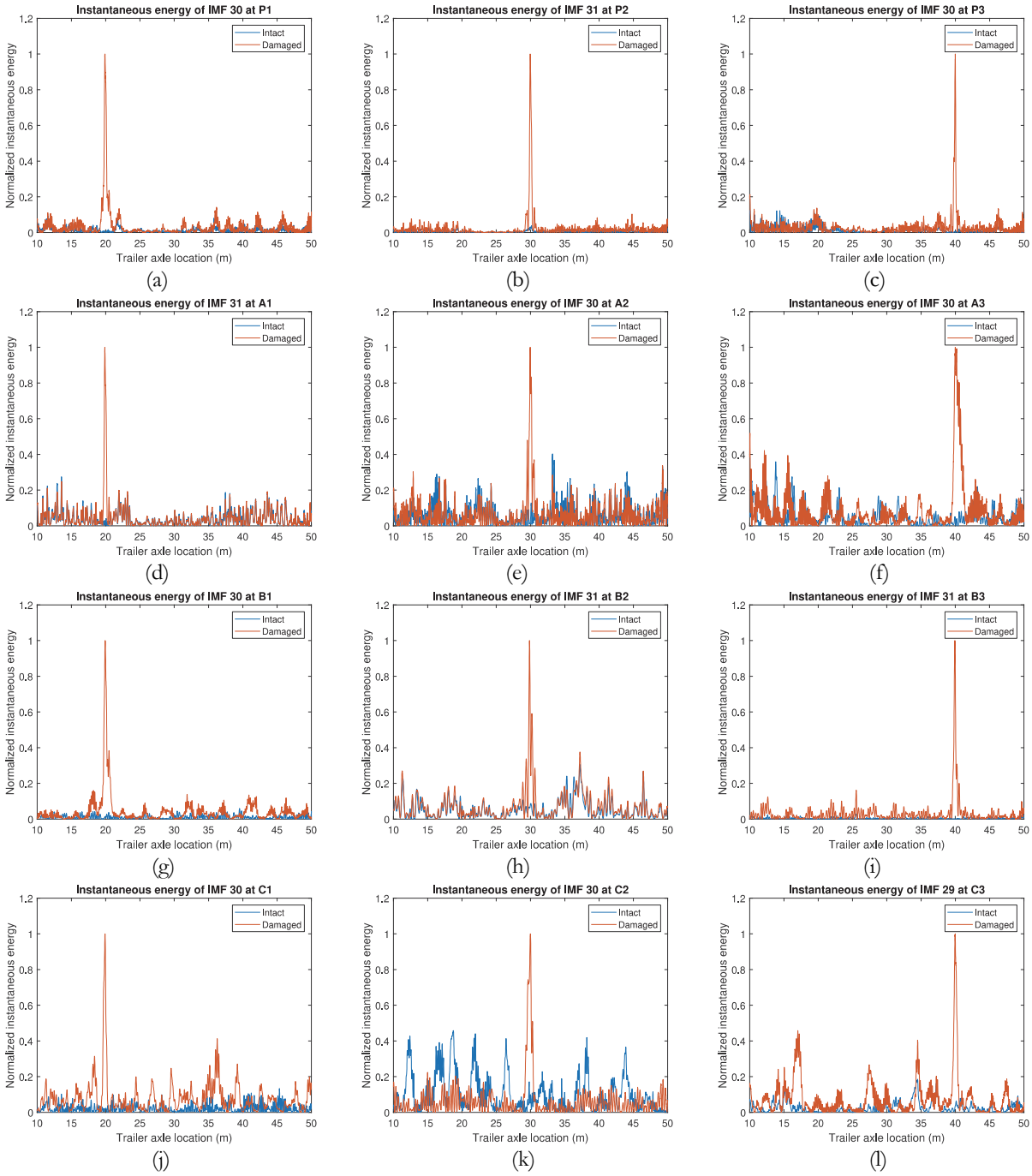

Figure 19: Normalized instantaneous energy of IMF extracted through VMD for cases (a) P1, (b) P2, (c) P3, (d) A1, (e) A2, (f) A3, (g) B1, (h) B2, (i) B3, (j) C1, (k) C2, (l) C3 with noise.

It is important to note that an SNR of 40 dB has been identified as an acceptable range for effective damage detection under the conditions tested in this study. Within this range, VMD effectively manages the noise, allowing for clear identification of damage locations. However, when the SNR falls below 40 dB, it becomes increasingly challenging to detect damages, especially in scenarios involving higher road roughness.

A comparison between EMD and VMD

According to the results acquired in the *Results and Discussions* section, the damages cannot be detected by implementing the EMD. The instantaneous energies of all modes decomposed by the EMD approach are given in Fig. 10, and it can be observed that the peaks seen in those diagrams do not coincide with the location of the damages. In fact, the EMD method

cannot be successfully used in detecting the damage location(s) in those cases. On the other hand, the VMD approach results have been demonstrated to be quite promising. The damage locations can be spotted by the VMD by breaking down the signal into a customizable number of modes. The VMD approach employs a wiener filter to effectively remove noise, helping identify damage location(s) amid the presence of the noise. The advantage of the VMD method over the EMD has also been proved in bearing fault diagnostics [75]. In addition, a comparison of these two methods for speech enhancement demonstrates that the VMD method is superior [76].

CONCLUSIONS

In this study a cost-effective indirect damage detection technique is introduced. In this method, VMD is implemented in drive-by sensing of bridges. The acquired moving mass signals are decomposed using VMD, and it is found that a reliable estimate of damage location(s) can be found via the proposed methodology. The effects of several influencing factors including road surface profile, damage severity, and noise are examined throughout this research. The main findings of this are summarized hereafter:

- Results of the exclusively developed finite element code for analyzing the TT bridge interactions are in promising agreement with the modal analysis solutions and can be used to reach the signals of interest including the bridge vibrations resulting from moving mass. This can be done by subtracting the absolute displacement of the trailer axle and the relative displacement of the trailer.
- A meticulous comparison of the frequency spectrum for damaged and healthy states gives clues about the frequency range at which the IMFs should be scrutinized. A clear gap is evident in the power spectrum of these signals within a specific frequency band.
- Comparison of the EMD and VMD methods showed the superiority of VMD over the EMD method in identifying the location of damages.
- The damage location(s) can be reached even in the presence of a rough road profile. However, the road surface irregularities impose limitations on the detectable flaw size. The acquired results show that in the case of a perfect surface and roughness class A, the VMD technique can be implemented to identify cracks of lengths down to 10% of beam depth, while in roughness Class B and C, the detectable cracks are limited to 20% of the beam's depth.
- The VMD technique is capable of handling intrinsic signal noise down to a signal-to-noise ratio (SNR) of 40 *dB*. However, when the SNR level drops below 40 *dB*, it becomes increasingly challenging to identify minor damages accurately.
- In contrast to previous studies, this research investigates the detection of shallower cracks and employs a more advanced vehicle system.

In conclusion, the findings from the VMD method showcase its exceptional potential as a robust damage detection technique, demonstrating its effectiveness even when subjected to adverse conditions, such as rugged road surfaces and ambient noise. This method stands out for its ability to detect damage without requiring reference data from a healthy state. Nonetheless, further research is underway to analyze the efficacy of this method in detecting different types of cracks and its applicability to various bridge systems.

Additionally, because this method has a good ability to handle noise and detect small abrupt changes in signals, it holds promise for use in real-world problems. Although implementing this method in real-world scenarios could be very challenging, this study proves its theoretical feasibility. It is, therefore, worth examining this approach in practical applications to fully understand its potential and limitations.

In addition to the numerous advantages offered by this method, there exists a limitation within this approach. Decomposing the signal into several modes requires expertise to determine an appropriate number of modes, as this can greatly influence central frequencies and efficacy in damage detection. We anticipate that future research will address this limitation, enabling the configuration of the number of modes without requiring specialized expertise.

APPENDIX A: VEHICLE VIBRATION MATRICES

The mass, damping and stiffness matrices in Eqn. (3) are as follows:

$$\mathbf{M}_T = \begin{bmatrix} I_0 & 0 & 0 & 0 & 0 & 0 \\ 0 & m_0 & 0 & 0 & 0 & 0 \\ 0 & 0 & m_1 & 0 & 0 & 0 \\ 0 & 0 & 0 & m_2 & 0 & 0 \\ 0 & 0 & 0 & 0 & m_{t0} & 0 \\ 0 & 0 & 0 & 0 & 0 & m_{t1} \end{bmatrix} \tag{A1}$$

$$\mathbf{C}_T = \begin{bmatrix} c_1b_1^2 + c_2b_2^2 & c_1b_1 - c_2b_2 & -c_1b_1 & c_2b_2 & 0 & 0 \\ c_1b_1 - c_2b_2 & c_1 + c_2 & -c_1 & -c_2 & 0 & 0 \\ -c_1b_1 & -c_1 & c_1 + c_3 & 0 & 0 & 0 \\ c_2b_2 & -c_2 & 0 & c_2 + c_4 & 0 & 0 \\ 0 & 0 & 0 & 0 & c_{t1} & -c_{t2} \\ 0 & 0 & 0 & 0 & -c_{t2} & c_{t1} + c_{t2} \end{bmatrix} \tag{A2}$$

$$\mathbf{K}_T = \begin{bmatrix} k_1b_1^2 + k_2b_2^2 & k_1b_1 - k_2b_2 & -k_1b_1 & k_2b_2 & 0 & 0 \\ k_1b_1 - k_2b_2 & k_1 + k_2 & -k_1 & -k_2 & 0 & 0 \\ -k_1b_1 & -k_1 & k_1 + k_3 & 0 & 0 & 0 \\ k_2b_2 & -k_2 & 0 & k_2 + k_4 & 0 & 0 \\ 0 & 0 & 0 & 0 & k_{t1} & -k_{t2} \\ 0 & 0 & 0 & 0 & -k_{t2} & k_{t1} + k_{t2} \end{bmatrix} \tag{A3}$$

$$\boldsymbol{F}_T = \begin{pmatrix} 0 \\ 0 \\ k_3z_1 + c_3\dot{z}_1 \\ k_4z_2 + c_4\dot{z}_2 \\ 0 \\ k_{t2}z_3 + c_{t2}\dot{z}_3 \end{pmatrix} \tag{A4}$$

The parameter z in matrix Eqn. (A4) is as follows:

$$\begin{aligned} &z_1 = u(x_1,t) + r(x_1), \quad z_2 = u(x_2,t) + r(x_2), \quad z_3 = u(x_3,t) + r(x_3), \\ &\dot{z}_1 = \dot{u}(x_1,t) + r'(x_1)v, \quad \dot{z}_2 = \dot{u}(x_2,t) + r'(x_2)v, \quad \dot{z}_3 = \dot{u}(x_3,t) + r'(x_3)v \end{aligned} \tag{A5}$$

APPENDIX B: FREQUENCY SPECTRUM

The frequency spectrum for other damage cases (A1-A3, B1-B3, C1-C3) are shown as below figures.

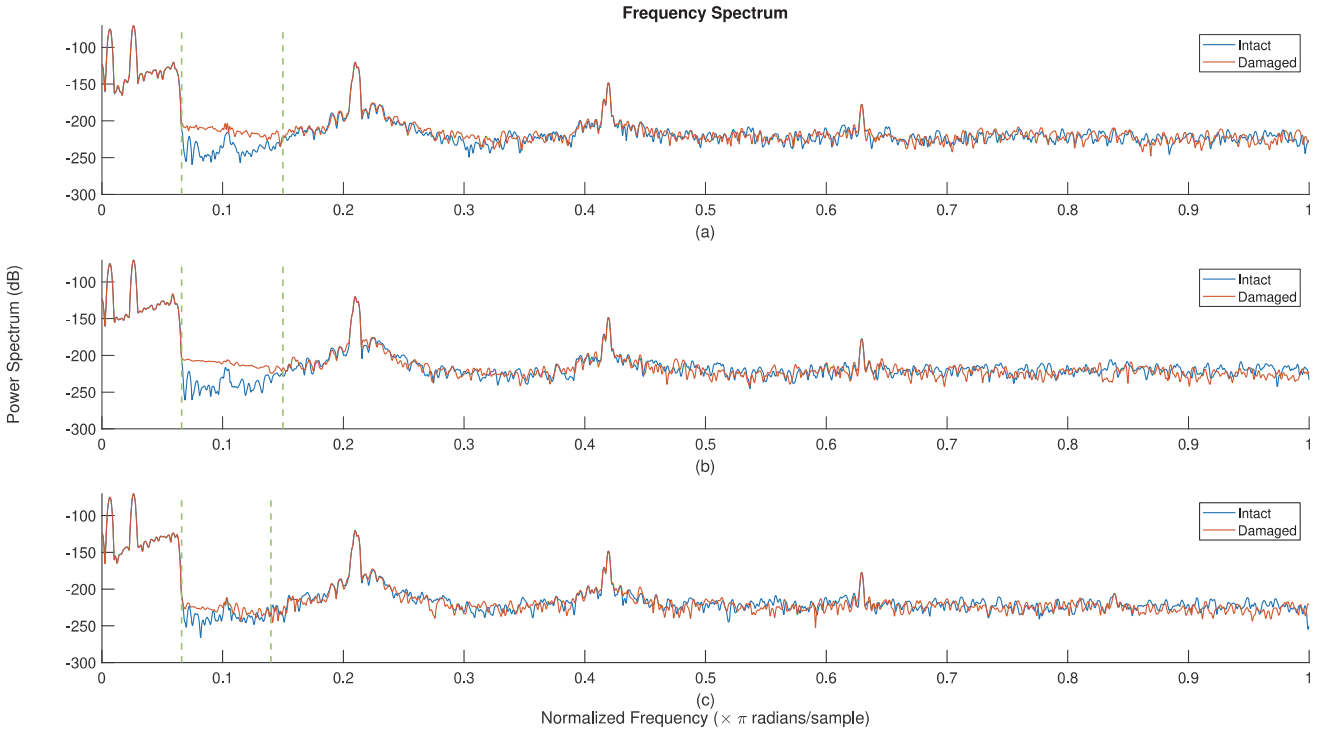

Figure B.1: Frequency spectrum for cases (a) A1, (b) A2, (c) A3.

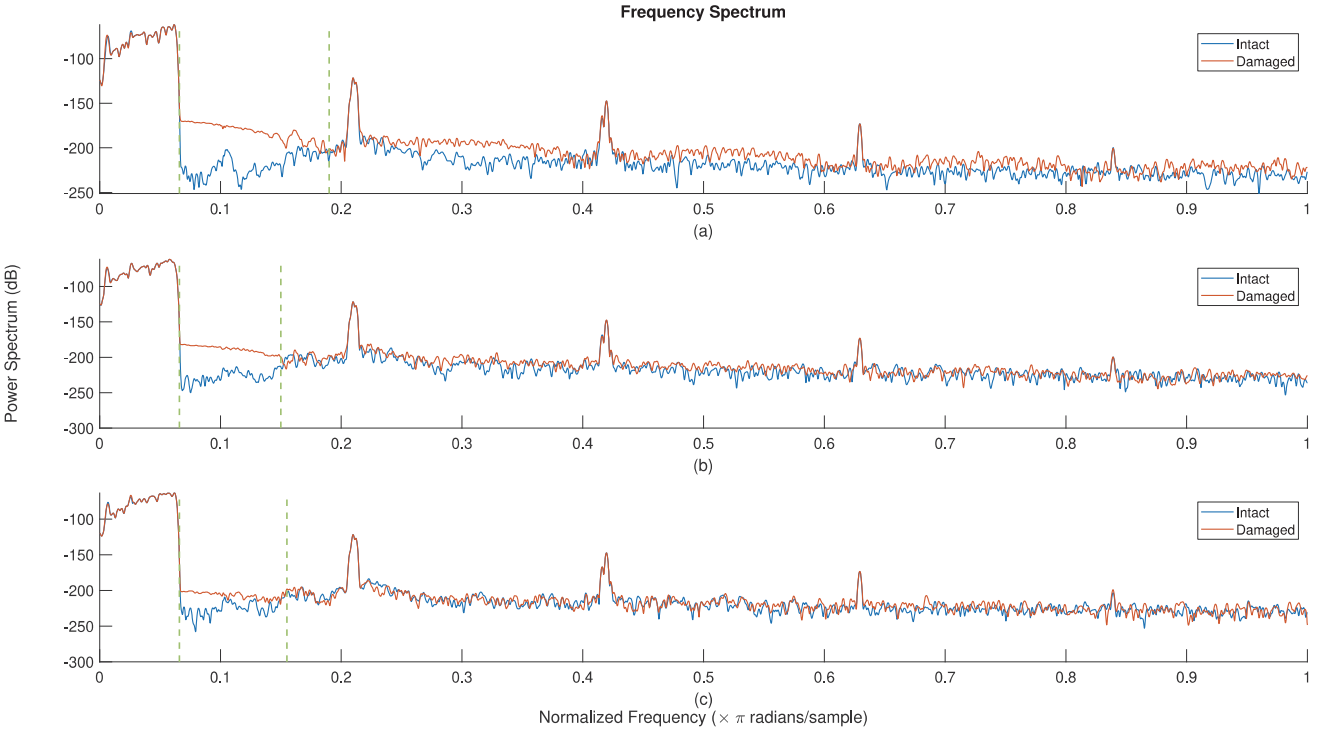

Figure B.2: Frequency spectrum for cases (a) B1, (b) B2, (c) B3.

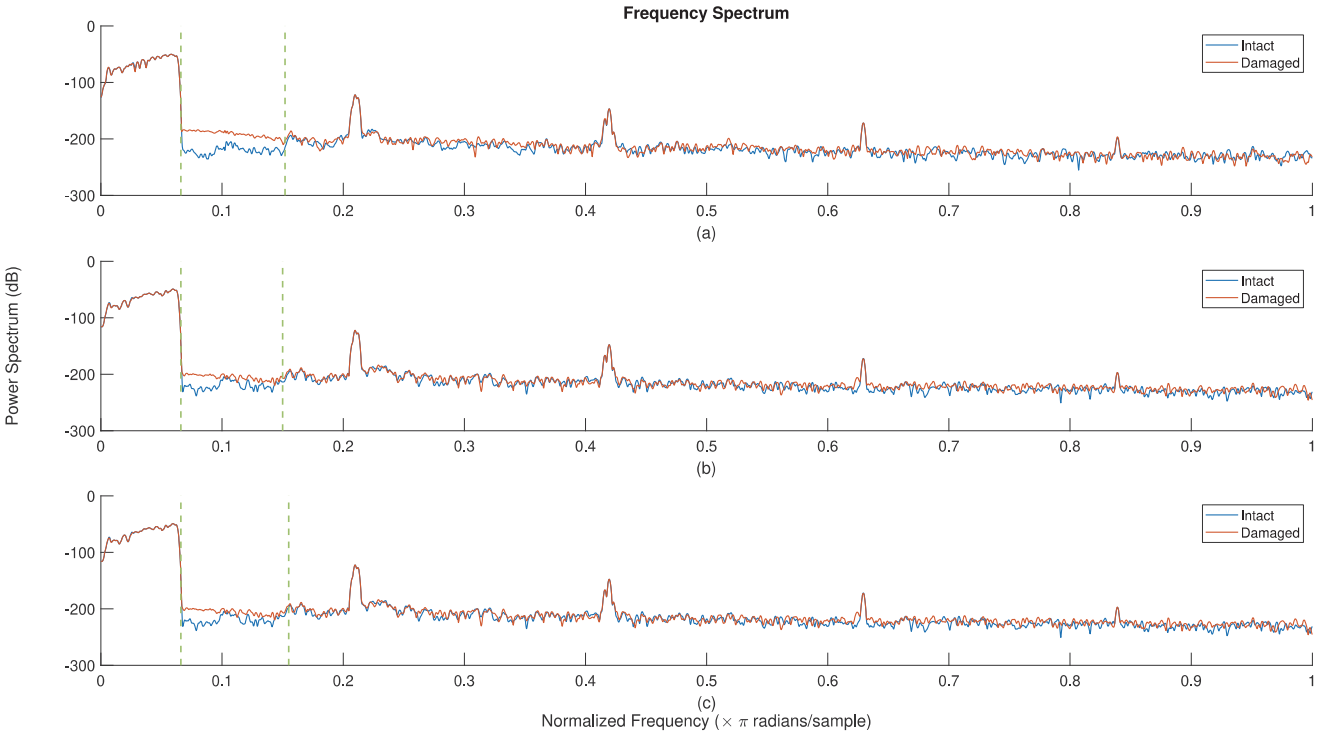

Figure B.3: Frequency spectrum for cases (a) C1, (b) C2, (c) C3.

REFERENCES

[1] Chupanit, P., Phromsorn, C. (2012). The Importance of Bridge Health Monitoring, International Journal of Civil and Environmental Engineering, 6(6), pp. 389–392. DOI: 10.5281/zenodo.1083277.

[2] Doebling, S.W., Farrar, C.R., Prime, M.B., Shevitz, D.W. (1996). Damage identification and health monitoring of structural and mechanical systems from changes in their vibration characteristics: a literature review, Office of Scientific and Technical Information (OSTI). DOI: 10.2172/249299.

[3] Cruz, P.J.S., Salgado, R. (2009). Performance of vibration-based damage detection methods in bridges, Computer-Aided Civil and Infrastructure Engineering, 24(1), pp. 62–79. DOI: 10.1111/j.1467-8667.2008.00546.x.

[4] Chang, K.-C., Kim, C.-W. (2016). Modal-parameter identification and vibration-based damage detection of a damaged steel truss bridge, Engineering Structures, 122, pp. 156–173. DOI: 10.1016/j.engstruct.2016.04.057.

[5] Comanducci, G., Magalhães, F., Ubertini, F., Cunha, Á. (2016). On vibration-based damage detection by multivariate statistical techniques: Application to a long-span arch bridge, Structural Health Monitoring, 15(5), pp. 505–524. DOI: 10.1177/1475921716650630.

[6] Malekjafarian, A., McGetrick, P.J., OBrien, E.J. (2015). A review of indirect bridge monitoring using passing vehicles, Shock and Vibration. DOI: 10.1155/2015/286139.

[7] Rizzo, P., Enshaeian, A. (2021). Bridge health monitoring in the United States: A review, Structural Monitoring and Maintenance, 8(1), p. 1. DOI: 10.12989/smm.2021.8.1.001.

[8] Lee, U., Shin, J. (2002). A frequency response function-based structural damage identification method, Computers & Structures, 80(2), pp. 117–132. DOI: 10.1016/S0045-7949(01)00170-5.

[9] Azam, S.E., Chatzi, E., Papadimitriou, C. (2015). A dual Kalman filter approach for state estimation via output-only acceleration measurements, Mechanical Systems and Signal Processing, 60, pp. 866–886. DOI: 10.1016/j.ymssp.2015.02.001.

[10] Sun, L., Shang, Z., Xia, Y., Bhowmick, S., Nagarajaiah, S. (2020). Review of bridge structural health monitoring aided by big data and artificial intelligence: from condition assessment to damage detection, Journal of Structural Engineering, 146(5), p. 4020073. DOI: 10.1061/(ASCE)ST.1943-541X.0002535.

[11] Chatterjee, A. (2000). An introduction to the proper orthogonal decomposition, Current Science, pp. 808–817.

[12] Hassanabadi, M.E., Heidarpour, A., Azam, S.E., Arashpour, M. (2020). Recursive principal component analysis for model order reduction with application in nonlinear Bayesian filtering, Computer Methods in Applied Mechanics and Engineering, 371, p. 113334. DOI: 10.1016/j.cma.2020.113334.
[13] Azam, S.E., Rageh, A., Linzell, D. (2019). Damage detection in structural systems utilizing artificial neural networks and proper orthogonal decomposition, Structural Control and Health Monitoring, 26(2), p. e2288. DOI: 10.1002/stc.2288.
[14] Rageh, A., Azam, S.E., Linzell, D.G. (2020). Steel railway bridge fatigue damage detection using numerical models and machine learning: Mitigating influence of modeling uncertainty, International Journal of Fatigue, 134, p. 105458. DOI: 10.1016/j.ijfatigue.2019.105458.
[15] Santos, J.P., Cremona, C., Orcesi, A.D., Silveira, P., Calado, L. (2015). Static-based early-damage detection using symbolic data analysis and unsupervised learning methods, Frontiers of Structural and Civil Engineering, 9(1), pp. 1–16. DOI: 10.1007/s11709-014-0277-3.
[16] Yang, Y.-B., Lin, C.W., Yau, J.D. (2004). Extracting bridge frequencies from the dynamic response of a passing vehicle, Journal of Sound and Vibration, 272(3–5), pp. 471–493. DOI: 10.1016/S0022-460X(03)00378-X.
[17] Yang, Y.B., Lin, C.W. (2005). Vehicle–bridge interaction dynamics and potential applications, Journal of Sound and Vibration, 284(1–2), pp. 205–226. DOI: 10.1016/j.jsv.2004.06.032.
[18] Yang, Y.B., Li, Y.C., Chang, K.C. (2012). Using two connected vehicles to measure the frequencies of bridges with rough surface: a theoretical study, Acta Mechanica, 223(8), pp. 1851–1861. DOI: 10.1007/s00707-012-0671-7.
[19] Yang, Y.B., Chang, K.C. (2009). Extraction of bridge frequencies from the dynamic response of a passing vehicle enhanced by the EMD technique, Journal of Sound and Vibration, 322(4–5), pp. 718–739. DOI: 10.1016/j.jsv.2008.11.028.
[20] Kim, C.-W., Isemoto, R., Toshinami, T., Kawatani, M., McGetrick, P., O'Brien, E.J. (2011). Experimental investigation of drive-by bridge inspection., 5th International Conference on Structural Health Monitoring of Intelligent Infrastructure (SHMII-5).
[21] Toshinami, T., Kawatani, M., Kim, C. (2010). Feasibility investigation for identifying bridge's fundamental frequencies from vehicle vibrations., Proceedings of the Fifth International IABMAS Conference on Bridge Maintenance, Safety, Management and Life-Cycle Optimization, p. 108.
[22] Lin, C.W., Yang, Y.B. (2005). Use of a passing vehicle to scan the fundamental bridge frequencies: An experimental verification, Engineering Structures, 27(13), pp. 1865–1878. DOI: 10.1016/j.engstruct.2005.06.016.
[23] McGetrick, P.J., Gonzlez, A., OBrien, E.J. (2009). Theoretical investigation of the use of a moving vehicle to identify bridge dynamic parameters, Insight-Non-Destructive Testing and Condition Monitoring, 51(8), pp. 433–438. DOI: 10.1784/insi.2009.51.8.433.
[24] González, A., OBrien, E.J., McGetrick, P.J. (2012). Identification of damping in a bridge using a moving instrumented vehicle, Journal of Sound and Vibration, 331(18), pp. 4115–4131. DOI: 10.1016/j.jsv.2012.04.019.
[25] McGetrick, P., Kim, C.-W., O'Brien, E.J. (2010). Experimental Investigation of the Detection of Bridge Dynamic Parameters Using a Moiving Vehicle., 23rd KKCNN Symposium on Civil Engineering, Taipei.
[26] Kim, C.-W., Isemoto, R., McGetrick, P., Kawatani, M., O'Brien, E.J. (2014). Drive-by bridge inspection from three different approaches, Smart Structures and Systems, 13(5), pp. 775–796. DOI: 10.12989/sss.2014.13.5.775.
[27] Arora, V., Singh, S.P., Kundra, T.K. (2009). Damped model updating using complex updating parameters, Journal of Sound and Vibration, 320(1–2), pp. 438–451. DOI: 10.1016/j.jsv.2008.08.014.
[28] Malekjafarian, A., OBrien, E.J. (2014). Identification of bridge mode shapes using short time frequency domain decomposition of the responses measured in a passing vehicle, Engineering Structures, 81, pp. 386–397. DOI: 10.1016/j.engstruct.2014.10.007.
[29] Oshima, Y., Yamamoto, K., Sugiura, K. (2014). Damage assessment of a bridge based on mode shapes estimated by responses of passing vehicles, Smart Structures and Systems, 13(5), pp. 731–753. DOI: 10.12989/sss.2014.13.5.731.
[30] Yang, Y.B., Li, Y.C., Chang, K.C. (2014). Constructing the mode shapes of a bridge from a passing vehicle: a theoretical study, Smart Structures and Systems, 13(5), pp. 797–819. DOI: 10.12989/sss.2014.13.5.797.
[31] Malekjafarian, A., OBrien, E.J. (2017). On the use of a passing vehicle for the estimation of bridge mode shapes, Journal of Sound and Vibration, 397, pp. 77–91. DOI: 10.1016/j.jsv.2017.02.051.
[32] Tan, C., Zhao, H., OBrien, E.J., Uddin, N., Fitzgerald, P.C., McGetrick, P.J., Kim, C.-W. (2021). Extracting mode shapes from drive-by measurements to detect global and local damage in bridges, Structure and Infrastructure Engineering, 17(11), pp. 1582–1596. DOI: 10.1080/15732479.2020.1817105.
[33] Kong, X., Cai, C.S., Kong, B. (2016). Numerically extracting bridge modal properties from dynamic responses of moving vehicles, Journal of Engineering Mechanics, 142(6), p. 4016025. DOI: 10.1061/(ASCE)EM.1943-7889.000103.

[34] Bu, J.Q., Law, S.S., Zhu, X.Q. (2006). Innovative bridge condition assessment from dynamic response of a passing vehicle, Journal of Engineering Mechanics, 132(12), pp. 1372–1379. DOI: 0.1061/(ASCE)0733-9399(2006)132:12(1372).
[35] Kim, C.W., Kawatani, M. (2009). Challenge for a drive-by bridge inspection., Proceedings of the 10th International Conference on Structural Safety and Reliability, pp. 758–765.
[36] Esfetanaj, N.N., Nojavan, S. (2018). The use of hybrid neural networks, wavelet transform and heuristic algorithm of WIPSO in smart grids to improve short-term prediction of load, solar power, and wind energy., Operation of Distributed Energy Resources in Smart Distribution Networks, Elsevier, pp. 75–100. DOI: 10.1016/B978-0-12-814891-4.00004-7.
[37] Nguyen, K.V., Tran, H.T. (2010). Multi-cracks detection of a beam-like structure based on the on-vehicle vibration signal and wavelet analysis, Journal of Sound and Vibration, 329(21), pp. 4455–4465. DOI: 10.1016/j.jsv.2010.05.005.
[38] Hester, D., González, A. (2012). A wavelet-based damage detection algorithm based on bridge acceleration response to a vehicle, Mechanical Systems and Signal Processing, 28, pp. 145–166. DOI: 10.1016/j.ymssp.2011.06.007.
[39] Nguyen, K.V. (2015). Dynamic analysis of a cracked beam-like bridge subjected to earthquake and moving vehicle, Advances in Structural Engineering, 18(1), pp. 75–95. DOI: 10.1260/1369-4332.18.1.75.
[40] Nguyen, K.V. (2013). Comparison studies of open and breathing crack detections of a beam-like bridge subjected to a moving vehicle, Engineering Structures, 51, pp. 306–314. DOI: 10.1016/j.engstruct.2013.01.018.
[41] Yin, S.-H., Tang, C.-Y. (2011). Identifying cable tension loss and deck damage in a cable-stayed bridge using a moving vehicle, Journal of Vibration and Acoustics, 133(2). DOI: 10.1115/1.4002128.
[42] OBrien, E.J., Malekjafarian, A., González, A. (2017). Application of empirical mode decomposition to drive-by bridge damage detection, European Journal of Mechanics-A/Solids, 61, pp. 151–163. DOI: 0.1016/j.euromechsol.2016.09.009.
[43] ElHattab, A., Uddin, N., OBrien, E. (2017). Drive-by bridge damage detection using non-specialized instrumented vehicle, Bridge Structures, 12(3–4), pp. 73–84. DOI: 10.3233/BRS-170106.
[44] Li, J., Zhu, X., Law, S.-S., Samali, B. (2020). A two-step drive-by bridge damage detection using Dual Kalman Filter, International Journal of Structural Stability and Dynamics, 20(10), p. 2042006. DOI: 10.1142/S0219455420420067.
[45] Tan, C., Elhattab, A., Uddin, N. (2020). Wavelet-entropy approach for detection of bridge damages using direct and indirect bridge records, Journal of Infrastructure Systems, 26(4), p. 4020037. DOI: 10.1061/(ASCE)IS.1943-555X.000057.
[46] Kildashti, K., Alamdari, M.M., Kim, C.W., Gao, W., Samali, B. (2020). Drive-by-bridge inspection for damage identification in a cable-stayed bridge: Numerical investigations, Engineering Structures, 223, p. 110891. DOI: 10.1016/j.engstruct.2020.110891.
[47] Nikkhoo, A., Karegar, H., Karami Mohammadi, R., Hajirasouliha, I. (2021). An acceleration-based approach for crack localisation in beams subjected to moving oscillators, Journal of Vibration and Control, 27(5–6), pp. 489–501. DOI: 10.1177/1077546320929821.
[48] Wang, Y., Markert, R., Xiang, J., Zheng, W. (2015). Research on variational mode decomposition and its application in detecting rub-impact fault of the rotor system, Mechanical Systems and Signal Processing, 60, pp. 243–251. DOI: 10.1016/j.ymssp.2015.02.020.
[49] Diao, X., Jiang, J., Shen, G., Chi, Z., Wang, Z., Ni, L., Mebarki, A., Bian, H., Hao, Y. (2020). An improved variational mode decomposition method based on particle swarm optimization for leak detection of liquid pipelines, Mechanical Systems and Signal Processing, 143, p. 106787. DOI: 10.1016/j.ymssp.2020.106787.
[50] Lahmiri, S. (2016). A variational mode decompoisition approach for analysis and forecasting of economic and financial time series, Expert Systems with Applications, 55, pp. 268–273. DOI: 10.1016/j.eswa.2016.02.025.
[51] Bagheri, A., Ozbulut, O.E., Harris, D.K. (2018). Structural system identification based on variational mode decomposition, Journal of Sound and Vibration, 417, pp. 182–197. DOI: 10.1016/j.jsv.2017.12.014.
[52] Zhang, M., Xu, F. (2019). Variational mode decomposition based modal parameter identification in civil engineering, Frontiers of Structural and Civil Engineering, 13(5), pp. 1082–1094. DOI: 10.1007/s11709-019-0537-3.
[53] Yang, Y.B., Xu, H., Mo, X.Q., Wang, Z.L., Wu, Y.T. (2021). An effective procedure for extracting the first few bridge frequencies from a test vehicle, Acta Mechanica, 232(3), pp. 1227–1251. DOI: 10.1007/s00707-020-02870-w.
[54] Mousavi, M., Holloway, D., Olivier, J.C., Gandomi, A.H. (2021). Beam damage detection using synchronisation of peaks in instantaneous frequency and amplitude of vibration data, Measurement, 168, p. 108297. DOI: 10.1016/j.measurement.2020.108297.
[55] Barbosh, M., Singh, P., Sadhu, A. (2020). Empirical mode decomposition and its variants: a review with applications in structural health monitoring, Smart Materials and Structures, 29(9), p. 93001. DOI: 10.1088/1361-665X/aba539.

[56] Huang, N.E., Shen, Z., Long, S.R., Wu, M.C., Shih, H.H., Zheng, Q., Yen, N.-C., Tung, C.C., Liu, H.H. (1998). The empirical mode decomposition and the Hilbert spectrum for nonlinear and non-stationary time series analysis, Proceedings of the Royal Society of London. Series A: Mathematical, Physical and Engineering Sciences, 454(1971), pp. 903–995. DOI: 10.1098/rspa.1998.0193.
[57] Yu, D., Cheng, J., Yang, Y. (2005). Application of EMD method and Hilbert spectrum to the fault diagnosis of roller bearings, Mechanical Systems and Signal Processing, 19(2), pp. 259–270. DOI: 10.1016/S0888-3270(03)00099-2.
[58] Yu, L., Wang, S., Lai, K.K. (2008). Forecasting crude oil price with an EMD-based neural network ensemble learning paradigm, Energy Economics, 30(5), pp. 2623–2635. DOI: 10.1016/j.eneco.2008.05.003.
[59] Guo, Z., Zhao, W., Lu, H., Wang, J. (2012). Multi-step forecasting for wind speed using a modified EMD-based artificial neural network model, Renewable Energy, 37(1), pp. 241–249. DOI: 10.1016/j.renene.2011.06.023.
[60] Dragomiretskiy, K., Zosso, D. (2013). Variational mode decomposition, IEEE Transactions on Signal Processing, 62(3), pp. 531–544. DOI: 10.1109/TSP.2013.2288675.
[61] Liu, W., Cao, S., Chen, Y. (2016). Applications of variational mode decomposition in seismic time-frequency analysis, Geophysics, 81(5), pp. V365–V378. DOI: 10.1190/geo2015-0489.1.
[62] Huang, N.E. (2014). Hilbert-Huang transform and its applications, 16, World Scientific. DOI: 10.1142/8804.
[63] OBrien, E.J., Keenahan, J. (2015). Drive-by damage detection in bridges using the apparent profile, Structural Control and Health Monitoring, 22(5), pp. 813–825. DOI: 10.1002/stc.1721.
[64] OBrien, E.J., Malekjafarian, A. (2016). A mode shape-based damage detection approach using laser measurement from a vehicle crossing a simply supported bridge, Structural Control and Health Monitoring, 23(10), pp. 1273–1286. DOI: 10.1002/stc.1841.
[65] OBrien, E.J., Martinez, D., Malekjafarian, A., Sevillano, E. (2017). Damage detection using curvatures obtained from vehicle measurements, Journal of Civil Structural Health Monitoring, 7(3), pp. 333–341. DOI: 10.1007/s13349-017-0233-8.
[66] Lin, Y.-H., Trethewey, M.W. (1990). Finite element analysis of elastic beams subjected to moving dynamic loads, Journal of Sound and Vibration, 136(2), pp. 323–342. DOI: 10.1016/0022-460X(90)90860-3.
[67] Paz, M., Kim, Y. H. (2019). Structural Dynamics: Theory and Computation, Springer International Publishing. DOI: 10.1007/978-3-319-94743-3.
[68] Youcef, K., Sabiha, T., El Mostafa, D., Ali, D., Bachir, M. (2013). Dynamic analysis of train-bridge system and riding comfort of trains with rail irregularities, Journal of Mechanical Science and Technology, 27(4), pp. 951–962. DOI: 10.1007/s12206-013-0206-8.
[69] Nikkhoo, A., Hassanabadi, M.E., Azam, S.E., Amiri, J.V. (2014). Vibration of a thin rectangular plate subjected to series of moving inertial loads, Mechanics Research Communications, 55, pp. 105–113. DOI: 10.1016/j.mechrescom.2013.10.009.
[70] Tada, H., Paris, P.C., Irwin, G.R. (2000). The Stress Analysis of Cracks Handbook, Third Edition, ASME Press. DOI: 10.1115/1.801535.
[71] Qian, G.-L., Gu, S.-N., Jiang, J.-S. (1990). The dynamic behaviour and crack detection of a beam with a crack, Journal of Sound and Vibration, 138(2), pp. 233–243. DOI: 10.1016/0022-460X(90)90540-G.
[72] Kam, T.-Y., Lee, T.Y. (1992). Detection of cracks in structures using modal test data, Engineering Fracture Mechanics, 42(2), pp. 381–387. DOI: 10.1016/0013-7944(92)90227-6.
[73] ISO, I. (1995). Mechanical vibration—Road surface profiles—Reporting of measured data, ISO 8608.
[74] Agostinacchio, M., Ciampa, D., Olita, S. (2014). The vibrations induced by surface irregularities in road pavements–a Matlab® approach, European Transport Research Review, 6(3), pp. 267–275. DOI: 10.1007/s12544-013-0127-8.
[75] Mohanty, S., Gupta, K.K., Raju, K.S. (2014). Comparative study between VMD and EMD in bearing fault diagnosis., 2014 9th International Conference on Industrial and Information Systems (ICIIS), pp. 1–6. DOI: 10.1109/ICIINFS.2014.7036515.
[76] Ram, R., Mohanty, M.N. (2017). Comparative analysis of EMD and VMD algorithm in speech enhancement, International Journal of Natural Computing Research (IJNCR), 6(1), pp. 17–35. DOI: 10.4018/IJNCR.2017010102.

NOMENCLATURE

$\boldsymbol{u}_k$: intrinsic mode function (IMF)

$\boldsymbol{\omega}_k$: central frequency of IMF

$\boldsymbol{\lambda}$: Lagrange multiplier
α : variance of white noise
δ : Dirac delta function
ω_n : desired IMF frequency
H : Hilbert transform function
$\mathbf{M_T}$: mass matrix of truck–trailer
$\mathbf{C_T}$: damping matrix of truck–trailer
$\mathbf{K_T}$: stiffness matrix of truck–trailer
$\boldsymbol{d}$: node displacement
$\mathbf{M}$: mass matrix of bridge
$\mathbf{C}$: damping matrix of bridge
$\mathbf{K}$: stiffness matrix of bridge
$\mathbf{N}$: shape function
$\boldsymbol{f}_1$: interaction force at rear axle of truck
$\boldsymbol{f}_2$: interaction force at front axle of truck
$\boldsymbol{f}_t$: interaction force at trailer axle
$\hat{\boldsymbol{f}}_1, \hat{\boldsymbol{f}}_2, \hat{\boldsymbol{f}}_3$: forces due to inertia of truck–trailer and trailer axles
$\boldsymbol{f}_{\theta 1}, \boldsymbol{f}_{\theta 2}$: forces due to moment of rotational inertia of truck–trailer
$\boldsymbol{u}$: vertical displacement
$\boldsymbol{g}$: acceleration due to gravity
a : crack depth in damaged element
b : beam height
b_1, b_2, b_3 : distance between axles
c_1,c_2,c_{t1} : damping of shock absorber between truck-trailer body and axles
c_3,c_4,c_{t2} : damping of wheels of truck-trailer
k_1,k_2,k_{t1} : stiffness of spring between truck-trailer body and axles
k_3,k_4,k_{t2} : stiffness of wheels of truck-trailer
I : moment of inertia
I_0 : mass moment of inertia
m_0 : mass of truck
m_1, m_2, m_{t1} : mass of axles of truck-trailer
m_{t0} : mass of trailer
L : length of bridge span
$\boldsymbol{f}(t)$: original signal
E : Elastic Modulus under normal conditions
E' : Elastic Modulus in Plane Strain conditions
v : Poisson's ratio
$G_d(n)$: power spectral density function
K_I, K_{II}, K_{III} : stress intensity factors of modes
$\boldsymbol{R}_{wk}$: force due to weight
$\boldsymbol{F}_{wk}$: force due to inertia
$\boldsymbol{w}(x,t)$: beam displacement in modal analysis
W^0 : strain energy of intact beam
W^1 : strain energy of cracked beam
$\boldsymbol{\phi}_j$: mode shape
q_j : generalized coordinate
$\boldsymbol{v}$: vehicle velocity
$r(x)$, $r'(x)$: Surface roughness function, derivative of surface roughness function

$\boldsymbol{S}$: clean signal
$\boldsymbol{Sn}$: noisy signal
z_1, z_2, z_3 : total vertical displacement of axles
$\hat{z}_1, \hat{z}_2, \hat{z}_3$: total vertical velocity of axles